

AD-A253 377



**Defense Nuclear Agency
Alexandria, VA 22310-3398**



DNA-TR-90-223

**Comparison of HOB Curves for 0.5-g NP Charges
with Field Test Data and Calculations**

**Heinz Reichenbach
Günther Scheklinski-Glück
Ernst Mach Institut
Fraunhofer-Institut für Kurzezeitdynamik
Eckerstrasse 4
D-7800 Freiburg, Germany**

**Logicon RDA
P.O. Box 92500
Los Angeles, CA 90009**

July 1992

Technical Report



CONTRACT No. DNA 001-88-C-0046

**Approved for public release;
distribution is unlimited.**

92-18845



92 7 15 045

Destroy this report when it is no longer needed. Do not return to sender.

PLEASE NOTIFY THE DEFENSE NUCLEAR AGENCY,
ATTN: CSTI, 6801 TELEGRAPH ROAD, ALEXANDRIA, VA
22310-3398, IF YOUR ADDRESS IS INCORRECT, IF YOU
WISH IT DELETED FROM THE DISTRIBUTION LIST, OR
IF THE ADDRESSEE IS NO LONGER EMPLOYED BY YOUR
ORGANIZATION.



DISTRIBUTION LIST UPDATE

This mailer is provided to enable DNA to maintain current distribution lists for reports. (We would appreciate your providing the requested information.)

- Add the individual listed to your distribution list.
- Delete the cited organization/individual.
- Change of address.

NOTE:
Please return the mailing label from the document so that any additions, changes, corrections or deletions can be made easily.

NAME: _____

ORGANIZATION: _____

OLD ADDRESS	CURRENT ADDRESS
_____	_____
_____	_____
_____	_____

TELEPHONE NUMBER: () _____

DNA PUBLICATION NUMBER/TITLE	CHANGES/DELETIONS/ADDITIONS, etc.) <small>(Attach Sheet if more Space is Required)</small>
_____	_____
_____	_____
_____	_____

DNA OR OTHER GOVERNMENT CONTRACT NUMBER: _____

CERTIFICATION OF NEED-TO-KNOW BY GOVERNMENT SPONSOR (if other than DNA): _____

SPONSORING ORGANIZATION: _____

CONTRACTING OFFICER OR REPRESENTATIVE: _____

SIGNATURE: _____

CUT HERE AND RETURN



**DEFENSE NUCLEAR AGENCY
ATTN: TITL
6801 TELEGRAPH ROAD
ALEXANDRIA, VA 22310-3398**

**DEFENSE NUCLEAR AGENCY
ATTN: TITL
6801 TELEGRAPH ROAD
ALEXANDRIA, VA 22310-3398**

REPORT DOCUMENTATION PAGE

Form Approved
OMB No. 0704-0188

Public reporting burden for this collection of information is estimated to average 1 hour per response, including the time for reviewing instructions, searching existing data sources, gathering and maintaining the data needed, and completing and reviewing the collection of information. Send comments regarding this burden estimate or any other aspect of this collection of information, including suggestions for reducing this burden, to Washington Headquarters Services, Directorate for Information Operations and Reports, 1215 Jefferson Davis Highway, Suite 1204, Arlington, VA 22202-4302, and to the Office of Management and Budget, Paperwork Reduction Project (0704-0188), Washington, DC 20503.

1. AGENCY USE ONLY (Leave blank)		2. REPORT DATE 920701	3. REPORT TYPE AND DATES COVERED Technical 890101 - 910831	
4. TITLE AND SUBTITLE Comparison of HOB Curves for 0.5-g NP Charges with Field Test Data and Calculations			5. FUNDING NUMBERS C - DNA 001-88-C-0046 ✓ PE - 62715H PR - RD TA - RC WJ - DH880125	
6. AUTHOR(S) Heinz Reichenbach, Günter Scheklinski-Glück, (EMI) and Allen Kuhl (Logicon RDA Consultant)				
7. PERFORMING ORGANIZATION NAME(S) AND ADDRESS(ES) Ernst Mach Institut Fraunhofer-Institut für Kurzzeitdynamik Eckerstrasse 4 D-7800 Freiburg, GERMANY Logicon RDA P.O. Box 92500 Los Angeles, CA90009 ✓			8. PERFORMING ORGANIZATION REPORT NUMBER RDA-TR-2-6322-9003-001	
9. SPONSORING/MONITORING AGENCY NAME(S) AND ADDRESS(ES) Defense Nuclear Agency 6301 Telegraph Road Alexandria, VA 22310-3398 SPSP/Castleberry			10. SPONSORING/MONITORING AGENCY REPORT NUMBER DNA-TR-90-223	
11. SUPPLEMENTARY NOTES This work was sponsored by the Defense Nuclear Agency under RDT&E RMC Codes B4662D RD RC 00016 DFPR 1910A 25904D and B4662D RD RC 00021 DFPR 1910A 25904D.				
12a. DISTRIBUTION/AVAILABILITY STATEMENT Approved for public release; distribution is unlimited.			12b. DISTRIBUTION CODE	
13. ABSTRACT (Maximum 200 words) Experiments are described on the reflection of spherical blast waves from planar surfaces. The blast waves were created by the detonation of 0.5-g spherical charges of NITROPENTA (NP). The scale of the experiments was about 1/1000 per kiloton. Diagnostics included schlieren photography and a high-speed pressure measurement system. A parametric series of height-of-burst (HOB) experiments were conducted over hydrodynamically smooth, rough and porous surfaces. Peak pressure measurements were used to construct isobaric HOB curves. The NP curves agree with the HOB curves derived from field tests that utilized much larger HE charges (1 to 500 kg). Nevertheless, comparison with high-fidelity pressure measurements from point-explosion tests and recent hydrocode simulations of the same tests has demonstrated that peak pressures on the NP experiments are about 20 percent too low in the low-pressure transition region — due to gauge-size limitations. The waveforms become extremely peaked in this transition region, and gauges with better frequency response are needed to accurately measure the peak pressures.				
14. SUBJECT TERMS Height of Burst Curves Real Surface Effects Boundary Layers Scaling Point Explosions Von Neumann Two-Shock Theory			15. NUMBER OF PAGES 84	
			16. PRICE CODE	
17. SECURITY CLASSIFICATION OF REPORT UNCLASSIFIED	18. SECURITY CLASSIFICATION OF THIS PAGE UNCLASSIFIED	19. SECURITY CLASSIFICATION OF ABSTRACT UNCLASSIFIED	20. LIMITATION OF ABSTRACT SAR	

UNCLASSIFIED

SECURITY CLASSIFICATION OF THIS PAGE

CLASSIFIED BY:

N/A since Unclassified

DECLASSIFY ON:

N/A since Unclassified

PREFACE

This work was sponsored by the Defense Nuclear Agency (DNA) under contract number DNA 001-88-0046 to Logicon RDA and contract number DNA 001-88-C-0125 to the Ernst-Mach-Institut (EMI). The third author, Dr. Allen Kuhl, is a consultant to Logicon RDA and an employee of the Lawrence Livermore National Laboratory (LLNL). Part of his work is performed under the auspices of the U.S. Department of Energy by LLNL under contract W-7405-ENG-48 and DNA IACRO number 91-853 and Work Unit 00354. Dr. Paul Castleberry was the DNA Project Officer. We are thankful to him and Dr. George W. Ullrich for their interest and support of this work.

We would like to acknowledge the contributions of Dip. Ing. Schetzler and Herr Gehri who performed the experiments at EMI, and Herr H.P. Mehlin (EMI) who manufactured the NP charges. Their attention to detail and their dedication to scientific methods allowed us to make accurate and consistent measurements at such a small scale. We would also like to thank Frau S. Deschoux (EMI) and Ms. V. Fox (RDA) for typing the numerous drafts of this manuscript, and Ms. E. Garnholz (RDA) for her excellent artwork on the figures.

We also acknowledge the many discussions of this work with other scientists, in particular: Mr. F.M. Sauer (RRA) who pointed out the difficulty of measuring the very peaked waveforms in the transition region, and who provided additional unpublished data and comparisons; Mr. H.J. Carpenter (CRC) who reviewed a vast amount of poor point-explosion data and found the accurate and reliable data (NOL measurements) used in our comparisons; he also provided a critical review of this work, and constructive recommendations in regard to the miniature PCB gauges; Prof. P. Colella (Univ. of California, Berkeley), for his clarification of the Neumann Reflection phenomenon; Prof. J. Dewey (Univ. of Victoria) for his review and encouragements; and Mr. R.F. Smiley (Kaman Avidyne), who provided the REFLECT code results. Their information contributed to the completeness of the comparisons described here, and their critiques have helped to highlight the key technical issues.

CONVERSION TABLE

Conversion factors for U.S. customary to metric (SI) units of measurement

(Symbols of SI units given in parentheses in middle column)

To convert from	To	Multiply by
angstrom (Å)	meters (m)	$1.000\ 000 \times 10^{-10}$
atmosphere (normal)	kilo pascal (kPa)	$1.013\ 25 \times 10^2$
bar	kilo pascal (kPa)	$1.000\ 000 \times 10^2$
barn	meters (m ²)	$1.000\ 000 \times 10^{-28}$
British thermal unit (thermochemical)	joule (J)	$1.054\ 350 \times 10^3$
calorie (thermochemical)	joule (J)	4.184 000
cal (thermochemical)/cm ²	mega joule/m ² (MJ/m ²)	$4.184\ 000 \times 10^{-2}$
curie	giga Becquerel (GBq)*	$3.700\ 000 \times 10^1$
degree (angle)	radian (rad)	$1.745\ 329 \times 10^{-2}$
degree Fahrenheit (°F)	degree kelvin (K)	$T_K = (T_F + 459.67)/1.8$
electron volt	joule (J)	$1.602\ 19 \times 10^{-19}$
erg	joule (J)	$1.000\ 000 \times 10^{-7}$
erg/second	watt (W)	$1.000\ 000 \times 10^{-7}$
foot	meter (m)	$3.048\ 000 \times 10^{-1}$
foot-pound-force	joule (J)	1.355 818
gallon (U.S. liquid)	meter ³ (m ³)	$3.785\ 412 \times 10^{-3}$
inch	meter (m)	$2.540\ 000 \times 10^{-2}$
jerk	joule (J)	$1.000\ 000 \times 10^9$
joule/kilogram (J/kg) (radiation dose absorbed)	Gray (Gy)**	1.000 000
kilotons	tera joules	4.183
kip (1000 lbf)	newton (N)	$4.448\ 222 \times 10^3$
kip/inch ² (ksi)	kilo pascal (kPa)	$6.894\ 757 \times 10^3$
ktap	newton-second/m ² (N-s/m ²)	$1.000\ 000 \times 10^2$
micron	meter (m)	$1.000\ 000 \times 10^{-6}$
mil	meter (m)	$2.540\ 000 \times 10^{-5}$
mile (international)	meter (m)	$1.609\ 344 \times 10^3$
ounce	kilogram (kg)	$2.834\ 952 \times 10^{-2}$
pound-force (lbf avoirdupois)	newton (N)	4.448 222
pound-force inch	newton-meter (N-m)	$1.129\ 848 \times 10^{-1}$
pound-force/inch	newton/meter (N/m)	$1.751\ 268 \times 10^2$
pound-force/foot ²	kilo pascal (kPa)	$4.788\ 026 \times 10^{-2}$
pound-force/inch ² (psi)	kilo pascal (kPa)	6.894 757
pound-mass (lbm avoirdupois)	kilogram (kg)	$4.535\ 924 \times 10^{-1}$
pound-mass-foot ² (moment of inertia)	kilogram-meter ² (kg-m ²)	$4.214\ 011 \times 10^{-2}$
pound-mass/foot ³	kilogram/meter ³ (kg/m ³)	$1.601\ 846 \times 10^1$
rad (radiation dose absorbed)	Gray (Gy)**	$1.000\ 000 \times 10^{-2}$
roentgen	coulomb/kilogram (C/kg)	$2.579\ 760 \times 10^{-4}$
shake	second (s)	$1.000\ 000 \times 10^{-8}$
slug	kilogram (kg)	$1.459\ 390 \times 10^1$
torr (mm Hg, 0° C)	kilo pascal (kPa)	$1.333\ 22 \times 10^{-1}$

* The Becquerel (Bq) is the SI unit of radioactivity; 1 Bq = 1 event/s.

** The Gray (Gy) is the SI unit of absorbed radiation.

TABLE OF CONTENTS

Section		Page
	PREFACE	iii
	CONVERSION TABLE	iv
	LIST OF ILLUSTRATIONS	vi
1	INTRODUCTION	1
2	EXPERIMENT DESCRIPTION	3
3	SMOOTH-SURFACE RESULTS	6
4	COMPARISON WITH OTHER HE DATA	9
5	BOUNDARY LAYER EFFECTS	13
6	SCALING TO POINT EXPLOSIONS	17
7	COMPARISON WITH POINT-EXPLOSION DATA AND CALCULATIONS	21
8	CONCLUSIONS	26
9	RECOMMENDATIONS	29
10	LIST OF REFERENCES	32
	APPENDIX	65

DTIC QUALITY INSPECTED 2

Accession For	
NTIS GRA&I	<input checked="" type="checkbox"/>
DTIC TAB	<input type="checkbox"/>
Unannounced	<input type="checkbox"/>
Justification	
By _____	
Distribution/	
Availability Codes	
Dist	Avail and/or Special
A-1	

LIST OF ILLUSTRATIONS

Figure		Page
1	Schematic of the explosion chamber	34
2	Construction of NP charges: (a) spherical charge; (b) hemispherical charge; (c) mounting bracket for the hemispherical charge	35
3	Schematic of the photography system	35
4	Schematic of the pressure gauge mount.	36
5	Shadow photographs showing the blast reflection over the Makrolon surface for HOB=303 mm=3.8 m/kg ^{1/3} : (a) regular reflection structure near transition (GR=4.73 m/kg ^{1/3} , $\alpha = 51.2^\circ$, $\Delta_I = 4.1$ psi and $\Delta p_R \simeq 10$ psi); (b) Neumann reflection shock structure well past transition (GR=9.02 m/kg ^{1/3} , $\alpha = 67^\circ$, $\Delta p_I = 2$ psi and $\Delta p_R \simeq 5$ psi)	37
6	Pressure-range curves for 0.5-g NP charges (subscripts I and R denote incident and reflected values, respectively)	38
7	Peak-pressure height-of-burst curves for a hydrodynamically-smooth surface in the low-pressure regime: circles denote mean values, \pm denote $\pm 1\sigma$ uncertainty bands, stars denote extrapolated points	39
8	Peak-pressure height-of-burst curves for a hydrodynamically-smooth surface in the intermediate-pressure regime: notation is the same as Figure 7	40
9	Peak-pressure height-of-burst curves for a hydrodynamically-smooth surface in the high-pressure regime: notation is the same as Figure 7	41
10	Comparison of the NP height-of-burst curves for a smooth surface with data from 450-kg TNT charges ($\Delta p = 1$ to 15 psi)	42

LIST OF ILLUSTRATIONS (Continued)

Figure		Page
11	Comparison of the NP height-of-burst curves for a smooth surface with data from 450-kg TNT charges ($\Delta p = 9$ to 200 psi)	43
12	Comparison of the NP height-of-burst curves for a smooth surface with data from 1-kg RDX charges (symbol <i>X</i>)	44
13	Comparison of the NP data with the height-of-burst curves for 3.6-kg PBX-9404 charges	45
14	Peak-pressure height-of-burst curves for a smooth surface (symbol <i>O</i>), a rough surface (symbol <i>R</i>) and a porous surface (symbol <i>P</i>)	46
15	Peak-pressure decay with range for surface bursts: circles denote an ideal surface; squares denote an extrapolated surface burst	47
16	Ground range decrement, δ , versus ideal range	47
17	Peak-pressure height-of-burst curves for a smooth surface (symbol <i>O</i>) and an ideal surface (symbol <i>I</i>) in the intermediate-pressure regime	48
18	Peak-pressure height-of-burst curves for a smooth surface (symbol <i>O</i>) and an ideal surface (symbol <i>I</i>) in the low-pressure regime. The curves for $\Delta p = 2, 1.5$ and 1 psi are extrapolated	49
19	Comparison of reflected pressures on a deep snow surface (Wisotski, 1990) with the smooth-surface NP results (low-pressure regime)	50
20	Comparison of reflected pressures on a deep snow surface (Wisotski, 1990) with the smooth-surface NP results (intermediate-pressure regime)	51
21	Free-air peak pressure versus radius curve for point-source explosions (Smiley et al., 1981). Circles denote the NP free-air data points scaled by function SI^{Γ}	52

LIST OF ILLUSTRATIONS (Continued)

Figure		Page
22	Scale function, $SF = R_n/RNP$, versus shock radius, RNP , for NP charges	52
23	NP height-of-burst curves for a smooth surface (symbol O) and an ideal surface (symbol I) scaled to a 1-KT point explosion by function SF for $\Delta p = 1$ to 15 psi	53
24	NP height-of-burst curves for a smooth surface (symbol O) and an ideal surface (symbol I) scaled to a 1-KT point explosion by function SF for $\Delta p = 6$ to 200 psi	54
25	Comparison of the scaled NP height-of-burst curves with REFLECT code calculations of point-explosions (Smiley et al., 1981) for $\Delta p = 1$ to 15 psi	55
26	Comparison of the scaled NP height-of-burst curves with REFLECT code calculations of point-explosions (Smiley et al., 1981) for $\Delta p = 6$ to 200 psi	56
27	Comparison of the scaled NP height-of-burst curves with point explosion data, $\Delta p = 1$ to 15 psi	57
28	Comparison of the scaled NP height-of-burst curves with point explosion data, $\Delta p = 6$ to 200 psi	58
29	Peak pressure vs. range for a point explosion at $HOB = 600 \text{ ft}/KT^{1/3}$ from the REFLECT code calculations (Smiley et al., 1981)	59
30	Comparison of peak-overpressure vs. range curves for $HOB = 1056 \text{ ft}/KT^{1/3}$	60
31	Entropy contours showing the reflection of a point-source blast wave from a plane; $HOB = 1056 \text{ ft}/KT^{1/3} = 322 \text{ m}/KT^{1/3}$	61
A1	Height-of-burst reflection factors from the NP experiments performed over the smooth (Makrolon) surface	66

LIST OF ILLUSTRATIONS (Continued)

Figure		Page
A2	Comparison of the NP height-of-burst curves for positive phase impulse, I_+ , for a smooth surface vs. a porous surface	67
A3	Comparison of the NP height-of-burst curves for shock arrival time, TOA, for a smooth surface vs. a porous surface	68
A4	Comparison of the NP height-of-burst curves for positive phase duration, τ_+ , for a smooth surface vs. a porous surface	69

SECTION 1 INTRODUCTION

Information on the reflection of spherical blast waves is important for explosion safety analysis and for military applications. For example, one needs to know the peak pressure as a function of distance from an explosion and how it varies as a function of height of burst (HOB). Such information can be conveniently summarized as isobaric curves in the height of burst-ground range plane.

The transition region between regular reflection and Mach reflection is especially interesting from a gasdynamic point of view. The reflection process can lead to significant pressure enhancements in the low-pressure regime ($\Delta p \leq 1$ bar). These effects appear as extended "knees" in the isobaric HOB curves. The technical question is the extent of these "knees", and whether they might be influenced by real surface effects such as boundary layers and surface roughness.

Considerable information exists on the reflection of spherical blast waves from planar surfaces. In the low-pressure regime, HOB tests have been performed with 1-kg RDX spheres (Heilig et al., 1985) and with 1-kg TNT spheres (Kingery and Bulmash, 1984; Petes, 1986). In the high-pressure regime, HOB tests were conducted with 3.6-kg PBX-9404 spheres (Carpenter and Brode, 1974) and with 450-kg PENTOLITE spheres (Reisler et al., 1988). Because of charge size, these tests were necessarily performed outdoors and were, therefore, expensive, small in number, and subject to weather variations. Also, these studies did not systematically investigate real-surface effects on the transition process.

This paper describes a series of small-scale HOB experiments developed at the Ernst-Mach Institut (Reichenbach and Kuhl, 1989). The length scale of the experiments is approximately 1/1000 per kiloton. The advantages of such laboratory experiments are: (1) they are inexpensive, hence extensive parametric studies are feasible (e.g., we have conducted more than 700 HOB tests in nine months); (2) weather variations are eliminated (this is especially important in the low-pressure

regime); (3) the roughness of the reflecting surface is easily controlled; (4) high-fidelity photographic visualization is possible.

The experiments are described in Section 2. The results for a hydrodynamically-smooth surface are presented in Section 3 and compared with other HE test results in Section 4. The effects of surface roughness and porosity are described in Section 5. The NP data scaled to 1-KT conditions are shown in Section 6, and compared with data and hydrocode calculations in Section 7. Our conclusions and recommendations are presented in Sections 8 and 9.

SECTION 2

EXPERIMENT DESCRIPTION

The experiments were performed in the cubical explosion chamber (120-cm by 120-cm by 60-cm) depicted in Figure 1. This provided well-controlled ambient conditions, and protected personnel and equipment from the effects of the explosions. The chamber was equipped with optical-quality windows (69-cm by 20-cm by 2-cm thick) for high-speed photography. The reflecting plane was located on a replaceable roof section of the chamber. Three different reflecting surfaces were used: (1) a hydrodynamically-smooth surface (Makrolon; surface roughness, $\epsilon < 0.1\mu\text{m}$); (2) a hydrodynamically-rough surface (#40 sandpaper: $\epsilon \simeq 400\mu\text{m} = 5 \times 10^{-3} \text{ m/kg}^{1/3} = 1 \text{ ft/KT}^{1/3}$); (3) a porous rough surface (1-cm thick Filtrokelit ceramic plate: $\epsilon \simeq 30\mu\text{m} = 3.8 \times 10^{-4} \text{ m/kg}^{1/3} = 0.08 \text{ ft/KT}^{1/3}$, and porosity = 24% by volume).

A new explosive was developed for the experiments. It consisted of extremely-fine-powdered NITROPENTA (NP) dissolved in a mixture of gun cotton and acetone. To produce a spherical charge with central ignition, the procedure shown in Figure 2a was developed. Two electrode wires were centered in a mandrel holder (i); a 10- μm diameter ignition wire was wrapped around them and fixed with a silver solution. The holder was dipped several times (ii-iv) into the explosive mixture, which had the consistency of honey, until an ellipsoidal shape was achieved (v). After drying, the mandrel was placed in a lathe and the charge was machined into a sphere of 1-cm diameter. Then the mandrel holder was removed (vi). This method allowed us to position the ignitor wire precisely at the center of the charge. The finished density of the charge was $1.40 \pm 0.05 \text{ g/cm}^3$. The finished charge mass was approximately 0.5-g; this gives a length scale factor of 12.6 to a kilogram charge, or 854 to a kiloton point explosion.

The surface-burst charges were constructed by a different method (Fig. 2b). A mold was used to cast 0.5-g hemispherical charges of NITROPENTA with a diameter of 1.26 cm. To avoid any perturbations on the blast wave, the electrode wires were

connected to the charge from below. To isolate the chamber from these high-voltage wires, a nonconducting, disposable baseplate of plexiglass was used. The electrode wires were fed through two holes in the baseplate to a small cavity provided for the ignitor wire. The cavity was filled with a few milligrams of pure NITROPENTA that acted as a booster, and then the charge was glued to the baseplate. Thus, the ignitor wire was positioned at the center of the base of the hemisphere. The baseplate was mounted in a disposable Delrin cylinder that could deform during the explosion. The entire assembly was emplaced in the chamber by means of a mounting bracket (Fig. 2c) that shock-isolated the reflecting surface from the stress waves produced by the charge. The disadvantage of this system was that two holes in the plexiglass baseplate created a preferential relief path for the stresses under the charge. This permitted significant cratering of the plexiglass, with a concomitant loss of approximately 25 percent of the energy from the blast wave (see Section 3).

The electrode wires served as the charge support system for the height-of-burst tests. The charge position was controlled within ± 0.1 mm by machined gauge blocks. The charge was fired by dumping about 50 joules energy from a 10 kV capacitor bank into the fine ignitor wire. This created an over-driven detonation wave that caused a complete and repeatable detonation of the entire charge mass. The timing and firing was controlled by a computer that also synchronized the pressure recording and photographic systems.

The single-frame photography system consisted of a single-spark light source (300-ns duration), two spherical mirrors (64-cm diameter, 400-cm focal length) which produced a parallel light beam through the test section, and an open-shutter camera (Fig. 3). This system gave high-quality shadow pictures. By placing a razor blade edge at the second focus, excellent schlieren photographs could also be produced.

Static pressure histories were measured at 13 ground ranges along the reflecting surface. Kistler transducers (type 603B) with charge amplifiers (type 5001) were used. The sensitive area of the gauges was about 3 mm in diameter, thus, wave-form features that were smaller than $3 \text{ m}/KT^{1/3}$ or $8 \text{ ms}/KT^{1/3}$ could not be resolved accurately. The data were recorded on a LeCroy digital transient recorder

(type 8837F) which had a sampling frequency of 10 MHz. The gauge output was filtered at 280 kHz; under normal-shock reflection conditions, this system had a rise time of 1 μ s without overshoot in the record. Special precautions were taken to shock-isolate each pressures gauge from the blast-induced vibrations in the reflecting plane, e.g., Figure 4 shows that no metal contact was allowed between the pressure gauge support and the roof.

The pressure measurements were systematically analyzed by the following procedure. For each experiment, the *measured* peak-pressures (i.e., without extrapolation) were tabulated as a function of ground range and scaled to sea-level conditions. Then the data were fit with a least-squares computer program to produce an analytic fit to the peak pressure-range curve for each height of burst. These analytic functions were fed into the HOB program that calculated the iso-overpressure ranges and plotted the data as height-of-burst curves.

Experiments were performed for 22 different heights of burst, starting with 0.5-g NP hemisphere surface bursts, and extending to heights of burst of 500 mm ($6.3 \text{ m/kg}^{1/3} \simeq 1400 \text{ ft/kT}^{1/3}$) relevant to the low-pressure regime. First, a baseline set of experiments was conducted using the Makrolon plate as a reflecting plane. This data served as a benchmark control case for a hydrodynamically-smooth surface. Then the test series was repeated over a rough surface (#40 sandpaper) and over a porous Filtrokelit plate—to investigate how boundary layer momentum losses and mass losses affect the HOB curves.

SECTION 3

SMOOTH-SURFACE RESULTS

Figure 5 presents shadow photographs of the blast wave reflection from the Makrolon surface in the low pressure regime ($HOB = 303 \text{ mm} = 3.8 \text{ m/kg}^{1/3}$). Figure 5a depicts the regular reflection of the incident shock I. Also shown is the backward-facing shock I_1 that is characteristic of HE-driven blast waves, and its reflection from the surface (shock R_1). Figure 5b depicts the shock structure after transition to Mach reflection; the Mach stem NR and the slipline SL are clearly visible. As will be discussed in Section 8, this is actually a Neumann reflection shock structure and not a classical 3-shock Mach configuration. Shock R' denotes the reflection of shock R from the chamber floor (recall that the tests were performed upside down). Secondary images of the shock structures are caused by the curved-shock effects.

Figure 6 presents the peak overpressures (Δp_R) measured at ground zero as a function of height of burst. Using normal shock reflection factors, this curve was "un-reflected" to create the incident pressure-range curve (Δp_I) for the NITROPENTA blast wave (see Eq. (10) for an analytic fit to this free-air curve).

Figure 7 depicts the peak-pressure height-of-burst curves for the hydrodynamically-smooth surface in the low-pressure regime ($\Delta p = 1$ to 15 psi). The circles denote the measured points, while the symbols "+" and "-" represent the $+1\sigma$ and -1σ uncertainty bands on each pressure-range curve (typically about ± 1 percent in range). The data scatter is extremely small, and there are so many data points that it is very easy to draw the HOB curves through the data. The long dashed line denotes the limit of measurement region; the 2, 1.5 and 1 psi curves were obtained by extrapolation; a larger chamber is needed to measure these low pressures. The short dashed dotted lines denote the HOB curves in the regular reflection region—as calculated from the von Neumann two-shock theory and the incident free-air curve of Figure 6. The experimental HOB curves compare well with the two-shock theory for about the first half of the regular reflection region, but in the transition region between regular and Mach reflection, the experimental curves fail systematically below the theoretical curves for pressures less than 15 psi.

For the surface burst case ($HOB = 0$), there are always two data points for each pressure level: the circle (the left-most point) denotes the measured pressure from the 0.5-g hemisphere experiments; the star (the right-most point) corresponds to an ideal surface burst. It was calculated from the NP free-air curve by multiplying the range by $2^{1/3}$ (i.e., an ideal-surface approximation). The measured surface burst pressures occur at a ground range of about 90 percent of the ideal-surface case, i.e., $GR_{SB}/GR_{ISB} = 0.90$; cubing this gives the explosion energy ratio: $E_{SB}/E_{ISB} = (GR_{SB}/GR_{ISB})^3 = 0.751$. Thus only about 75 percent of the chemical energy for the hemispheric surface-burst charge was available to drive the blast wave, and 25 percent of the energy was lost to the cratering process.

Figure 8 presents the height-of-burst curves for the hydrodynamically-smooth surface in the intermediate-pressure regime ($\Delta p = 8$ to 200 psi). The notation is the same as in the previous figure. Again the data scatter is extremely small, and the HOB curves are very smooth. Again we see that for low pressures, the experimental HOB curves are below the theoretical curves in the transition region, while for higher pressures the data is in agreement with the theory throughout most of the regular reflection regime.

The charge center for the lowest four HOB experiments was located at heights of 0.5, 1, 1.5 and 2 cm; these correspond to a surface tangent case and to heights of burst of 1, 1.5 and 2 charge diameters, respectively. Because these charges were so close to the reflecting plane, a shaped-charge or piston effect was created by the dense detonation products jetting along the surface. This piston effect caused the shock to bulge outward near the surface, and distorted the pressure-range curve. This "HE squish effect" appears as a bulge in the HOB curves for low burst heights $HOB < 3.3 \text{ cm} = 0.4 \text{ m/kg}^{1/3}$). Figure 8 shows that the squish effect is most prominent at high pressures, and decreases at larger ground ranges.

Figure 9 presents the height-of-burst curves for the hydrodynamically-smooth surface in high-pressure regime ($\Delta p = 100$ to 1000 psi). The notation is the same as in the previous figures. The "HE squish effect" is especially prominent in this figure. At these high pressures, the data are consistent with the two-shock theory in the regular reflection regime. The 200 psi data point at $HOB = 1.2 \text{ m/kg}^{1/3}$ is

especially supportive of this statement. However, more experiments at intermediate heights of burst are needed to accurately define the knees in the NP height-of-burst curves in the high-pressure regime.

SECTION 4 COMPARISONS WITH OTHER HE DATA

In this section we shall compare the NP height-of-burst curves with data taken on a variety of HE field tests performed at much larger scale. We used the same method of analysis for the HE field tests that we had used for the NP experiments; namely, the data were cube-root scaled to sea-level conditions and then peak- pressure versus ground range data were curve fit using a least- squares program. Then the analytic fits were interrogated to find the iso-overpressure ground ranges and compared with the NP height-of-burst curves.

The first set of HE data that we analyzed is listed in Table 1. The height-of-burst data came from the DIPOLE WEST tests using 450-kg charges of TNT and the MIGHTY MACH tests employing primarily 29-kg charges of PENTOLITE; both were performed over concrete pads. The surface-burst data came from tests employing much larger stacked TNT charges. In those cases, a considerable fraction of the energy was lost in the cratering process. Because the scatter was typically quite large in this data set, we did not take into account the energy differences between TNT and NITROPENTA.

Figures 10 and 11 compare this HE data set with our smooth- surface NP curves. At low pressures (Fig. 10), the HE data is in excellent agreement with our NP curves—not only in Mach reflection region (i.e., below the knees) but also in the transition region and at the knees of the curves. Most notable are the pressure levels of $\Delta p_R = 1, 1.5, 2$ and 4 psi. In the intermediate pressure regime (Fig. 11), the HE data are also consistent with the NP curves but the HE data have much more scatter, especially for pressures of $\Delta p_R = 8$ to 15 psi. At somewhat higher pressures ($\Delta p_R = 30$ to 70 psi), the HE data lie just inside the NP curves but follow their general shape. In fact, the NP curves are closer to the two-shock theory, especially near transition, than the large-charge data—perhaps because we used a hydrodynamically-smooth surface. Thus, these figures show that increasing the explosion length scale by a factor of 100 does not raise the knees of the height-of-burst curves in the low-pressure transition region (because of the overall system

Table 1. HE test data sources.

W (lb)	HOB (m/kg ^{1/3})	Charge	Event
	0	TNT	FLATTOP II, FLATTOP III, DPL 3, MIDDLEGUST I ¹
	.05	TNT	DIAL PACK, DPL 6A, DPL 6, PRAIRIE FLAT, MIXED CO. ¹
	.10	TNT	MIDDLEGUST II, MINEUNDER ¹
~ 1000	.205	TNT	Shot 10 (1969 SERIES) ¹
~ 1000	.28	TNT	Shot 9 (1969 SERIES) ¹
~ 40,000	.33	TNT	Shot 1A (DISTANT PLAIN) ¹
~ 1000	.58	TNT	Shot 8 (1969 SERIES) ¹
~ 1000	.91	TNT	Shot 1, Shot 2 (1969 SERIES) ¹
~ 40,000	.97	TNT	Shot 1 (DISTANT PLAIN) ¹
~ 1000	1.102	TNT	Shot 4 (1969 SERIES) ¹
~ 1000	1.38	TNT	Shot 3 (1969 SERIES) ¹
1040	1.73	TNT	Shot 17 (DIPOLE WEST) ^{1,2}
~ 1000	1.77	TNT	Shot 5 (1969 SERIES) ¹
~ 1000	2.26	TNT	Shot 6 (1969 SERIES) ¹
~ 1040	2.30	TNT	Shot 18 (DIPOLE WEST) ^{1,2}
~ 1000	2.70	TNT	Shot 7 (1969 SERIES) ¹
1040	3.42	TNT	Shot 24 (DIPOLE WEST) ^{1,2}
1040	3.45	TNT	Shot 19 (DIPOLE WEST) ^{1,2}
1040	4.60	TNT	Shot 20 (DIPOLE WEST) ^{1,2}
1040	4.60	TNT	Shot 23 (DIPOLE WEST) ^{1,2}
1086	5.03	TNT	Shot 6 (DIPOLE WEST) ¹
1040	5.49	TNT	Shot 21 (DIPOLE WEST) ^{1,2}
1040	5.52	TNT	Shot 22 (DIPOLE WEST) ^{1,2}
63	5.7	PENTOLITE	Shot 1 (MIGHTY MACH II) ²
218	7.7	PENTOLITE	Shot 1 (MIGHTY MACH IV) ²
64	7.72	PENTOLITE	Shot 1 (MIGHTY MACH III) ²
64	7.73	PENTOLITE	Shot 2 (MIGHTY MACH II) ²
64	7.77	PENTOLITE	Shot 1A (MIGHTY MACH III) ²
217	9.62	PENTOLITE	Shot 2 (MIGHTY MACH IV) ²
64	9.65	PENTOLITE	Shot 2 (MIGHTY MACH III) ²

Superscript: 1 denotes Carpenter (1978) data set

2 denotes Sauer (1990) data set

response). We infer from this comparison that our peak-pressure measurements are as accurate as those made on the large HE tests.

These observations are supported by more accurate HE data presented in Figure 12. Shown there are results of height-of-burst tests performed at the Ernst-Mach-Institut's test site at Wintersweiler with RDX spheres (Heilig et al., 1985; Scheklinski-Glück, 1990). Charge masses of 1-kg, 0.128-kg and 0.016-kg were used. We note that the RDX tests used the same pressure gauges (KISTLER 603B) and recording system that were used in the NP experiments. Although not quite as smooth and consistent, the RDX data are in agreement with the NP curves. Most notably, the RDX data also suggests that the height-of-burst curves begin to deviate from the two-shock theory well before the detachment angle (see, for example, the curves for $\Delta p_R = 8, 10$ and 15 psi). At intermediate pressures (e.g., $\Delta p_R = 15, 20$ and 30 psi), the RDX curves have slightly more pronounced knees. This is a subtle but discernible trend that may have been caused by enhanced resolution of the peak-pressure measurements on the RDX experiments. Thus, increasing the explosion length scale by a factor of 10, and using the same pressure measurement system (thereby increasing the temporal resolution by about 10), has little effect on the shape of the height-of-burst curves.

To check the NP curves in the high-pressure regime (100 to 1000 psi) we made comparisons with data taken on tests with 3.6-kg spheres of PBX-9404 (Carpenter and Brode, 1974). Figure 13 shows that the NP data are in excellent agreement with the PBX curves—especially for $\Delta p_R = 100, 150$ and 200 psi—both in the knee region near transition and in the HE squish region near the surface. For pressures greater than about 150 psi, the shock structure transitions to a double-Mach configuration when the detachment angle is reached, and double-peaked waveforms are created. Smaller pressure gauges are required to measure the details of such waveforms accurately.

In summary, we find that blast wave generated by the 0.5-kg NP charges is consistent and reproducible, and provides an excellent laboratory simulation of the HE-driven blast waves employed in large-scale field tests. The accuracy of the pressure measurements made in our NP experiments was similar to the accuracy of pressure

measurements made on HE field tests (e.g., the HE data always lies inside or on the NP height-of-burst curves for a given pressure level). Comparisons with the RDX data set indicates that knees of the curves could be somewhat more pointed. Experiments with smaller-diameter pressure gauges should be made to check this trend, and to more fully define the NP height-of- burst curves in the high-pressure regime.

SECTION 5 BOUNDARY LAYER EFFECTS

In this section we explore how boundary layer effects change the height-of-burst curves. Rough-wall boundary layer effects were evaluated by comparing the results of NP experiments conducted over #40 sandpaper surface (labeled "R") with the smooth-surface curves, as shown in Figure 14. The large surface roughness ($\epsilon = 400\mu\text{m} = 0.005 \text{ m/kg}^{1/3} = 1 \text{ ft/KT}^{1/3}$) used here caused no significant effect on the peak pressures in the regular reflection region or in the Mach reflection region below the knees of the curves. Surface roughness clipped or rounded off the sharp peaks in the transition region; this caused a small but systematic depression of the curves in the knee region.

The effects of mass loss due to surface porosity were evaluated by comparing the results of the NP experiments performed over the Filtrokelit surface (labeled "P") with the smooth-surface curves, as also shown in Figure 14.* Porosity caused more dramatic effects than surface roughness, especially in the knee region of the curves, and this effect increased at the lower pressures.

The above comparisons demonstrate that the surface boundary condition has a measurable effect on the the shape of knees of the height-of-burst curves. The smooth-surface curves are the highest, followed by the rough-surface curves, and the porous-surface curves are the lowest. By induction, then, one would expect that the inviscid-surface curves would be even higher than the smooth-surface curves. Such effects are consistent with boundary layer theory. According to the momentum integral for a boundary layer behind a shock, momentum loss due to wall drag and mass loss due to porosity both have the same negative boundary layer displacement effect (i.e., a weak rarefaction effect) on the near-surface flow. Apparently the porosity had a larger effect than the surface roughness. Height-of-burst experiments over rough surfaces should be extended to lower pressures.

*Comparison of height of burst curves for other blast wave parameters (e.g., impulse, shock arrival time and positive phase duration) can be found in the Appendix.

From photography on the DIPOLE WEST tests we know that the triple point trajectory is suppressed on a concrete surface in comparison to an ideal reflecting plane (formed in those tests by the symmetry plane between two simultaneous bursts). This suppression is no doubt caused by the boundary layer along the surface. Note that even our hydrodynamically-smooth surface created a boundary layer. We infer from this that the triple point trajectory is suppressed even on such a smooth surface (relative to the triple point trajectory over an inviscidly-ideal surface); surface roughness or porosity will further enhance this effect. Apparently, suppression of the triple point trajectory erodes the peak pressures and pulls in the knees of the height-of-burst curves, as demonstrated in Figure 14. Hence, boundary layer effects seem to be responsible for transition well before the detachment angle is achieved. But because the boundary layer suppresses the triple point trajectory, the Mach stem is not detectable in photography until well after the detachment angle is reached. This will be discussed more fully in Section 7.

Further evidence of boundary layer effects is provided by the fact that the height-of-burst curves, when extrapolated to the surface, do not agree with the ideal surface burst points—even when a hydrodynamically-smooth surface is used as a reflecting plane. This effect is demonstrated in Figure 15, which depicts the peak pressure versus range curves for the ideal-surface case (label *ISB*) and the extrapolated surface burst case (label *ESB*). Clearly, the extrapolated surface burst case decays more rapidly than the ideal-surface case. This can also be seen in the exponent of the curve fits to the data;

$$\Delta p_{ISB} = 9.59/GR^{1.734} \quad (1)$$

$$\Delta p_{ESB} = 10.96/GR^{1.850} \quad (2)$$

where $[\Delta p] = \text{bars}$, $[GR] = \text{m/kg}^{1/3}$ and $3.5 < GR (\text{m/kg}^{1/3}) < 10$. For convenience, the above relations may be written in a logarithmic form:

$$\log \Delta p_{ISB} = a_1 - b_1 \log(GR_{ISB}) \quad (3)$$

$$\log \Delta p_{ESB} = a_2 - b_2 \log(GR_{ESB}) \quad (4)$$

where $a_1 = 0.982$, $b_1 = 1.734$, $a_2 = 1.04$ and $b_2 = 1.85$.

Let us define the percent decrement in ground range to the same overpressure:

$$\delta \equiv 100(GR_{ISB} - GR_{ESB})/GR_{ISB} \quad (5)$$

Using the pressure-range curves (Eqs. 3 and 4), one can show that

$$\delta = 230(a_1 - a_2)/b_2 + 230(1 - b_1/b_2) \log GR_{ISB} \quad (6)$$

or, after inserting the constants, one finds

$$\delta = 7.2 + 14.6 \log(GR_{ISB}) \quad (3 \leq GR \leq 10) \quad (7)$$

In other words, the ground-range decrement increases logarithmically with range (see Fig. 16). It is plausible that this increase with range is caused by boundary layer momentum and energy losses because the surface area in contact with the hemispherical blast wave increases as the square of the shock radius.

One can try to remove such boundary layer effects from the NITROPENTA data by increasing the ground range of each data point for the smooth-surface case, according to Eq. 7. This then defines our approximation to the ideal-surface height-of-burst curves (symbol *I*) shown in Figures 17 and 18. The boundary layer corrections begin at a pressure of $\Delta p = 15$ psi and the corrections increase logarithmically with range. They extend the knees somewhat, but the ideal-surface curves still remain below the two-shock theory curves near transition. Clearly this correction cannot eliminate the triple point suppression, and therefore, it cannot fully remove the boundary layer effects on transition.

In summary, we believe that boundary layer effects cause the knees in the HOB curves to be pulled in and down in the low-pressure regime. They probably trigger an early transition, and suppress the triple point trajectory. Apparently this happens even for a hydrodynamically-smooth surface. Comparisons with inviscid hydrocode simulations of the reflection of the NP blast wave could help verify this assertion.

An additional boundary effect that is worth noting. Height-of-burst tests have been conducted over snow and concrete surfaces (Wisotski, 1990). Typically, 1-lb TNT

charges were detonated over a deep snow layer (18 to 127 cm). Pressure waveforms were measured at the snow surface. We scaled the peak-pressure measurements to sea-level conditions and plotted the peak-pressure versus range curves. These were used to construct height-of-burst curves, which are compared with our NP curves in Figures 19 and 20. These figures show that the HOB curves for snow are dramatically contracted relative to the NP curves (or the concrete-surface curves) for peak pressures of 30 psi to 3 psi. The blast wave compresses the snow surface which changes the effective angle between the incident shock and the reflecting plane, and thus creates a local rarefaction wave near the surface. Also, the blast wave performs work in compressing the snow, and thus the blast wave loses energy to the snow. This dramatically changes the height-of-burst curves. No doubt this effect depends on the depth of the snow layer. For more realistically scaled depths of the snow layer, this effect may be considerably reduced.

SECTION 6

SCALING TO POINT EXPLOSIONS

In this section we will scale the NITROPENTA height-of-burst curves to conditions appropriate to large-scale point explosions, and compare these results with other data and hydrocode simulations.

The fundamental input to the scaling procedure is the free-air pressure versus radius curve for a 1 kiloton* point explosion (Smiley et al., 1981) depicted in Figure 21. The analytic fit to this curve is as follows:

$$\log \Delta p_n = \begin{cases} 5.885 - 2.6 \log R_n & \text{for } 67 < R_n \leq 141 \\ 7.147 - 4.279 \log R_n + 0.51(\log R_n)^2 & \text{for } 141 < R_n \leq 1106 \\ 2.613 - 1.241 \log R_n & \text{for } 1106 < R_n \leq 2926 \end{cases} \quad (8)$$

where $[\Delta p] = \text{bars}$ and $[R] = \text{m}/\text{KT}^{1/3}$. Next, we calculate a local scale function, SF , which is defined as the point-source radius to a given pressure divided by the NITROPENTA radius to the same pressure:

$$SF \equiv R_n/R_{NP} \quad (9)$$

Here, R_n comes from Figure 21 (or Eq. 8) and R_{NP} comes from the NITROPENTA free-air curve (Fig. 6), or equivalently:

$$\log \Delta p_{NP} = \begin{cases} 1.047 - 2.289 \log R_{NP} & \text{for } 0.9 < R_{NP} \leq 2.45 \\ 0.954 - 2.253 \log R_{NP} + 0.427(\log R_{NP})^2 & \text{for } 2.45 < R_{NP} \leq 9.8 \\ 0.462 - 1.334 \log R_{NP} & \text{for } 9.8 < R_{NP} \leq 28 \end{cases} \quad (10)$$

*Recall that 1-KT $\equiv 10^{12}$ calories.

where $[\Delta p_{NP}] = \text{bars}$ and $[R_{NP}] = \text{m/kg}^{1/3}$. As shown in Figure 22, this scale function varies with distance:

$$SF = f(R_{NP}) = \begin{cases} 73.18 - 28.675 \log(R_{NP}) & \text{for } R_{NP} < 1.54 \\ 67.75 & \text{for } R_{NP} \geq 1.54 \end{cases} \quad (11)$$

The scale function starts with a value of 74.4 at high pressures, decreases to a value of 67.75 at about 60 psi, and then remains constant (total variation of about 10%). To provide a consistency check, this scale function was applied to the data points for the NP free-air curve (Fig. 6), and compared with the point-source free-air curve in Figure 21. The agreement is excellent (deviations of less than one percent), so clearly the scale function (Eq. 11) accurately transforms NP ranges to point-source ranges.

With the incident blast wave properties properly scaled, an inviscid (i.e., cube-root of charge energy) scaling procedure can now be defined for the reflected pressure. One assumes that the reflected pressure values depend on only two parameters: the incident shock pressure (which is only a function of the scaled shock radius) and the incident shock angle α with respect to the reflecting surface ($\alpha = \tan^{-1}\{GR/HOB\}$). Thus the scaling procedure reduces to the following relations:

$$R_n = R_{NP} \cdot SF(R_{NP}) \quad (12)$$

$$\alpha_n = \alpha_{NP} \quad (13)$$

This inviscid scaling preserves the geometric similarity between the two blast waves. Hence, both the ground range and height of burst of any data point i on the NITROPENTA HOB curves may be scaled to an equivalent point for a point-source blast wave, according to:

$$GR_n(i) = GR_{NP}(i) \cdot SF[R_{NP}(i)] \quad (14)$$

$$HOB_n(i) = HOB_{NP}(i) \cdot SF[R_{NP}(i)] \quad (15)$$

where

$$R_{NP}(i) = \sqrt{GR_{NP}(i)^2 + HOB_{NP}(i)^2}$$

Clearly, this scaling neglects real-surface effects such as boundary layers.

Figures 23 and 24 present the height-of-burst curves for 1-KT point explosions, constructed from Figures 17 and 18 by means of the aforementioned inviscid scaling procedure. There are two curves for each pressure level: the curve with the "O" symbols represent the smooth-surface case, and the curve with the "I" symbols represent our approximation to the ideal-surface case (i.e., where the boundary layer decrement effects have been removed before scaling). Even after applying the scale function, the curves remain smooth and self-consistent.

In closing, it is worth pointing out that the cube-root scaling procedure employed here is based on inviscid similarity theory for blast waves (Sedov, 1959). It is theoretically valid only if the two blast waves can be matched with a *single scale constant*; for example, scaling results of an x-kg charge to those of a y-kg charge of the *same explosive*, or scaling results of an x-KT point explosion to those of a y-KT point explosion. Thus, the variable scale function SF used here has no firm theoretical basis. In fact, similarity scaling does not even work perfectly for all HE blast wave parameters; for example, the cube-root-scaled positive phase duration of TNT blast waves is different from those of more energetic explosives such as PBX-9404 (because TNT afterburns significantly and PBX does not). Fortunately, the pressure-range curve for most explosives is somewhat insensitive to these effects at low pressures and their pressure-range curves can be collapsed by scaling the data with the cube-root of the yield.

Besides this pedantic point, there are a number of physical effects that cannot be scaled. For example, when the reflected shock passes through the fireball, it heats the gas due to shock compression and changes its entropy. The irreversible part of this local energy change is then not available to drive the blast wave. Now, an HE fireball is 10 to 100 times more dense than the fireball of a point explosion, so a different fraction of the blast wave mass (and thus energy) will be affected in the two examples. Also, point explosions are not constant energy blast waves (because of radiation losses from the high-temperature fireball), whereas HE explosions produce blast waves of constant or increasing energy (due to afterburning). In addition, the density gradient of the atmosphere can refract the blast wave of large-yield point

explosions, and hydrocode calculations have shown that this can affect the height-of-burst curves for $\Delta p_R \leq 2$ psi. Finally, boundary layer effects—especially in the transition region—cannot be scaled.

In summary, there is no scaling theory that properly accounts for all the physical effects. Hence, the variable scale function SF employed here represents the best available engineering approximation for comparing HE results with those of point explosions.

SECTION 7

COMPARISON WITH POINT EXPLOSION DATA AND CALCULATIONS

Next we shall compare our NP curves with the results of inviscid hydrocode simulations of the reflection of point explosion blast waves from an inviscid surface. Calculations were performed with the REFLECT code (Smiley et al., 1981), and the results were intended to serve as converged solutions for the ideal-surface case. Figures 25 and 26 present the comparisons. At low pressures, the REFLECT code results lie between our smooth-surface and ideal-surface curves in the Mach reflection region — especially at the surface (i.e., the surface burst values). This indicates that we have properly scaled the NP data. The major difference appears in the transition region. The height-of-burst curves from the REFLECT code (denoted by the dashed lines) follow the two-shock theory all the way to the detachment condition, and then bulge upward and outward relative to the NP curves. This trend is prominent for reflected pressures of $\Delta p_R \leq 30$ psi.

Figure 27 compares our scaled NP curves with data from field tests of large point explosions; the typical yields were about 20 KT (see Table 2 for specific events). One can see that the data generally agree with our curves in the low-pressure Mach reflection regime (e.g., the 4 psi curve), but the data scatter is quite large.

Figure 28 presents similar comparisons for intermediate pressures. In a review of a preliminary version of our NP data, F. Sauer pointed out that the Tumbler-Snapper series had some high-quality pressure measurements at the right ground ranges and heights of burst (Event 1 at HOB = 754 ft/KT^{1/3}, Event 2 at HOB = 1009 ft/KT^{1/3}, and Event 3 at HOB = 1055 ft/KT^{1/3}) to clarify the shape of the knees in the transition region for $\Delta p_R = 6$ to 10 psi. Subsequently, H.J. Carpenter has confirmed that the NOL measurements on these events were indeed of high quality, and he re-analyzed the peak-pressure versus range curves. Using these data, we have constructed the curve labeled NOL in Figure 28. At $\Delta p = 6$ psi,

Table 2. Point explosion data sources.

SHOB (ft)	EVENT
0	Koa (HARDTACK I) ¹
0	Mike (IVY) ¹
2.3	Butternut (HARDTACK I) ¹
2.7	Koon (CASTLE) ¹
3.1	Sugar (JANGLE) ¹
95	Harry (UPSHOT-KNOTHOLE) ¹
113	Annie (UPSHOT-KNOTHOLE) ¹
138	Met (TEAPOT) ¹
143	Humboldt (HARDTACK II) ¹
156	Apple II (TEAPOT) ¹
182	King (IVY) ¹
196	Apple I (TEAPOT) ¹
204	Priscilla (PLUMBBOB) ¹
205	Grable (UPSHOT-KNOTHOLE) ¹
205	Yuma (REDWING) ¹
212	Galileo (PLUMBBOB) ¹
220	Wilson (PLUMBBOB) ¹
239	Morgan (PLUMBBOB) ¹
241	Bee (TEAPOT) ¹
322	Climax (UPSHOT-KNOTHOLE) ¹
340	Hood (PLUMBBOB) ¹
368	Dog (TUMBLER-SNAPPER) ¹
397	Easy (BUSTER) ¹
446	Charlie (BUSTER) ¹
488	Ruth (UPSHOT-KNOTHOLE) ¹
489	Dog (BUSTER) ¹
502	Hamilton (HARDTACK II) ¹
554	Franklin (PLUMBBOB) ¹
633	Charleston (PLUMBBOB) ¹
692	Wasp (TEAPOT) ¹
702	Baker (BUSTER) ¹
754	Able (TUMBLER-SNAPPER) ^{1,2}
786	Encore (UPSHOT-KNOTHOLE) ¹
831	Rushmore (HARDTACK II) ¹
1009	Baker (TUMBLER-SNAPPER) ^{1,2}
1055	Charlie (TUMBLER-SNAPPER) ^{1,2}
1092	Eddy (HARDTACK II) ¹
1133	Mora (HARDTACK II) ¹
1249	Lea (HARDTACK II) ¹
2565	Dixie (UPSHOT-KNOTHOLE) ¹

Superscript: 1 denotes Carpenter (1978) data set

2 denotes Sauer (1990) data set

this curve falls halfway between the NP curve and the REFLECT code curve. We believe that this indicates that the NP measurements missed the peak due to gauge-size effects, and the REFLECT code results overshoot the peak due to grid constraints.

To verify these statements, we have examined a REFLECT code calculation of a $HOB = 600 \text{ ft}/KT^{1/3}$. The calculated pressure-range curve is shown in Figure 29. The peak pressures decay with range and agree with the two-shock theory for the entire regular reflection region — until the detachment angle α_d is reached. Then the pressures climb rapidly until a triple point (denoted by TP) is first observed in the calculation; subsequently the peaks decay rapidly as the Mach shock structure becomes better resolved on the mesh. This local peak can dramatically change the calculated range-to-effect; for example, the ground range to $\Delta p_R = 30 \text{ psi}$ is increased from $460 \text{ ft}/KT^{1/3}$ to $680 \text{ ft}/KT^{1/3}$ because of this effect. This tendency for the pressure to increase at transition is not observed in any of the data nor in other hydrocode simulations. Hence, we suspect that this local peak may be an artifice of the formulation of the REFLECT code calculation.

The REFLECT code is a first-order Godunov scheme that uses front tracking techniques for all shocks. The incident blast wave is solved on a one-dimensional grid. The flowfield inside the reflected shock is solved on a two-dimensional grid that conforms to the shape of the reflected shock. The two domains interact via the jump conditions across the reflected shock. The shock jump relations are also used to advance each local piece of the reflected shock. At the reflection point a triangular cell is used. The state inside that cell is determined by applying the two-shock theory (given the incident shock strength and angle). Hence, it is clear that the method of calculation forces the REFLECT code results to agree with the two-shock theory throughout the regular reflection domain. Near transition, the topology of the grid is changed to that of a Mach reflection structure. The REFLECT code specifies that the state in the quadrilateral cell located at the triple point is determined by applying the three-shock theory. When the Mach stem is less than one cell high [i.e., for ground ranges from $GR(\alpha_d)$ to $GR(TP)$], this method forces the pressure to be too large. Therefore, we believe grid constraints in the REFLECT code could

be the cause of dramatic increases in peak pressure at transition that are not found in the data or other (unconstrained) hydrocode calculations.

As another illustration, we present the pressure-vs-range data for Tumbler-Snapper 3 ($HOB = 1056 \text{ ft}/KT^{1/3}$) in Figure 30. The curve labeled FS is Fred Sauer's best estimate for this event as predicted by his construction factor method. The curve labeled NOL corresponds to H.J. Carpenter's evaluation of the NOL pressure records. The curve labeled NP comes from our scaled NP height-of-burst curves. It traces a lower bound of all the data from Tumbler (where the lower values of peak pressure come typically from gauges with poorer response). Also shown in Figure 30 are results of an AMR calculation of a blast wave reflection from an inviscid surface (Ferguson, 1990). The coarse-zoned calculation ($\Delta_{\min} = 10 \text{ ft}/KT^{1/3}$) gave peak pressures in agreement with the NP curve (gauge size $\simeq 8 \text{ ft}/KT^{1/3}$), while the fine-zoned calculation ($\Delta_{\min} = 1 \text{ ft}/KT^{1/3}$) gave peak pressures that were consistent with the NOL curve (gauge size $\simeq 0.3 \text{ ft}/KT^{1/3}$). We infer from this that the gauges on the NP tests were too large in diameter to accurately measure these peaks at transition.

Figure 31 depicts the entropy contours at various times from the aforementioned fine-zoned AMR calculation of the reflection of a point-explosion blast wave from an inviscid surface ($HOB = 1056 \text{ ft}/KT^{1/3} = 322 \text{ m}/KT^{1/3}$). Entropy was selected as the display variable because it is the most sensitive indicator of a contact surface emanating from a triple point. The contour plots show the transition from a regular reflection shock structure to a Mach reflection shock structure. An entropy layer begins to appear along the wall at a GR $\simeq 280 \text{ m} = 919 \text{ ft}$ ($\alpha = 41^\circ$) and is clearly defined at a GR = $388 \text{ m} = 1273 \text{ ft}$ ($\alpha = 50^\circ$). Eventually the entropy layer lifts off the wall and an identifiable Mach stem is observed, e.g., GR $\simeq 630 \text{ m} = 2067 \text{ ft}$ ($\alpha = 63^\circ$). If one defines transition as the formation of an entropy layer near the surface, then this calculation indicates that transition occurs at an $\alpha = 41^\circ$ to 50° , while the theoretical detachment angle for this case is $\alpha_d = 57^\circ$. Hence, this inviscid AMR calculation indicates that the shock structure transitions well before the detachment condition is reached.

As the Mach stem evolves, the gradient in entropy from the triple-point region (i.e., the contact surface) weakens and then disappears, e.g., GR = 1052 m = 3451 ft ($\alpha = 73^\circ$). The shock structure appears to be similar to the Neumann Reflection NR structure described by Henderson and Colella (1990) for weak shock reflections from wedges. Recall that for a NR structure, the outer shock is continuously curved (i.e., there is no kink at the triple point) and the reflected shock spreads out into a dispersed wave near the front. Thus, the triple point becomes a dispersed wave region devoid of any contact surface or slipline. Notice also in Figure 31, that the gradients behind the reflection point are much steeper than the gradients in the incident blast wave. Thus, one needs a much finer mesh or much smaller gauges to accurately capture peaks for such Neumann Reflections (compared to what would be needed to resolve the incident blast wave).

To summarize, the above comparisons suggest that the REFLECT code results overshoot at transition due to grid constraints. The NP experiments missed the peak at transition because of gauge-size effects; hence, smaller gauges ($\leq 1 \text{ ft}/KT^{1/3} = 0.36 \text{ mm}/.5 \text{ g}^{1/3}$) are needed to accurately measure such peaks. Fortunately, PCB has recently developed smaller pressure gauges that may significantly improve the peak pressure measurements (see Section 9). The AMR results were consistent with the NOL data and show that although the overpressure does not locally peak near transition, the pressure-range curve does flatten and lead to more pronounced knees in the low pressure HOB curves than indicated by the NP data. These calculations also showed that the shock structure transitions to a dispersed wave system in the low-pressure regime.

SECTION 8 CONCLUSIONS

1. NP Height-of-Burst Curves.

Measurements made on the 0.5-g NP experiments form a very extensive and self-consistent height-of-burst data set. Because the NP data is self-consistent (i.e., the same charge, the same gauges and the same surface were used), one can detect subtle effects such as boundary layer effects.

The shape of the NP height-of-burst curves agrees with data from height-of-burst experiments performed with much larger HE charges. The NP data are also consistent with the low fidelity (i.e., poor response) point explosion data. Nevertheless, comparison with high fidelity point explosion data (e.g., the NOL data) and recent AMR hydrocode calculations has demonstrated that the NP peak pressures are about 20% too low in the low-pressure transition region — due to gauge-size limitations. Hence, smaller gauges (or larger explosions) are needed to more-accurately define the peak pressures in the transition region.

2. NR Shock Structure.

According to recent hydrocode simulations, the reflected shock structure transitions to a Neumann Reflection (NR)—not a classical three-shock Mach structure—for weak shock reflections. This is confirmed by photography (in Fig. 5). There is a strong rarefaction wave associated with this NR structure which causes a steep pressure gradient behind the foot of the Mach stem and makes it difficult to resolve the peak (experimentally or computationally).

3. Transition Criterion.

The transition criterion *is not known for weak blast waves*. According to pressure measurements on HE experiments (Figs. 9, 10 and 11) and point explosion tests, the transition seems to occur (i.e., reflected pressures start to deviate from the

two-shock theory) before the detachment angle α_d is reached: $\alpha_T \simeq 40^\circ$ ($\Delta p_R = 30$ psi) and $\alpha_T \simeq 28^\circ$ ($\Delta p_R = 8$ psi). It is not known whether this is a gasdynamic effect or a boundary layer effect, or whether it is caused by measurement inaccuracies.

4. Boundary Layer Effects.

Boundary layer effects on peak reflected pressures were estimated from the data taken on the hydrodynamically-smooth surface. Negligible effects were found at small ground ranges. However, boundary layer effects probably caused a deficit in range to the same overpressure that increased logarithmically with ground range:

$$\delta(\%) = 7.2 + 14.6 \log(GR)$$

for peak pressures below 15 psi. The effects of the boundary layer on the transition ground range could not be evaluated; comparisons with inviscid-surface hydrocode calculations are required for that purpose.

5. Other Real-Surface Effects.

Rough-wall boundary layer effects were evaluated from the pressure data taken on the #40 sandpaper surface by comparison with the smooth-surface results. No effect on the peak pressures was found in the regular reflection region. A slight decrease in the ground range for transition was observed. After transition, a small but systematic depression of the peak pressures was measured in the knee region of the curves. Below the knee region, the large roughness had essentially no effect on the peak pressure HOB curves.

The effects of mass loss due to surface porosity were evaluated from the pressure data taken on the Filtrokelit surface. Porosity caused no effect on the peak pressures in the regular reflection region. Porosity had some effect on the ground range to transition, and this effect increased at lower pressures and higher burst heights. The large porosity employed in these tests dramatically modified the height-of-burst curves from transition to the knee region, but below the knee region, porosity had no effect on the curves.

The effects of surface compressibility were evaluated from the pressure data taken over a deep snow layer (Wisotski, 1990). Dramatic changes to all portions of the height-of-burst curves were observed for all reported pressures ($\Delta p_R = 3$ to 30 psi). This may be a deep-snow effect that would be reduced if a scaled snow depth is used.

SECTION 9 RECOMMENDATIONS

We offer the following recommendations for improvements to the experimental technique, additional tests to explore real-surface effects, and supporting hydrocode calculations.

1. Smaller Pressure Gauges.

Smaller-diameter pressure gauges* all needed to accurately measure the very peaked waveforms in the low-pressure transition region and to investigate the double-peaked waveforms in the double-Mach reflection in the high-pressure regime. First, shock tube tests should be performed with such small gauges mounted next to the Kistler 603B gauges. This will allow direct comparisons of the recorded pressures measured at the same position on the same test, by which we can evaluate potential improvements in measured rise times and peak values. Side-on tests, end-wall tests and wedge-reflection tests are also needed. Then, the smaller gauges can be used in future HOB tests.

2. Larger Explosion Chamber.

Currently the HOB curves for $\Delta p = 1, 1.5$ and 2 psi are based on extrapolations of the pressure-range curves. A larger explosion chamber ($\sim 2\text{m}$ by 2m by 1.5m) should be built so that the low-pressure HOB curves can be constructed from measurements—not extrapolations.

3. Photography of Mach Reflection Transition.

Shadow-schlieren photography should be used to systematically investigate the shock structure in the transition region. This can be used to estimate Mach transition.

*For example, the PCB Corporation has recently developed crystal gauges with a sensitive element of 0.015 inches across, which have an output of hundreds of millivolts per psi.

4. High-Pressure HOB Curves.

Additional tests with intermediate HOBs and ground ranges are needed to more fully define the NP height-of-burst curves in the high-pressure region ($\Delta p = 100$ to 1000 psi).

5. Real-Surface Effects.

The height-of-burst tests should be continued to produce a complete set of NP height-of-burst curves (i.e., down to pressures of $\Delta p_R = 1$ psi) for both hydrodynamically smooth and rough surfaces.

In addition, height-of-burst tests should be performed over other nonideal surfaces, for example: Astro-Turf carpet could be used to simulate shock diffraction effects caused by forests and vegetation, polyurethane foam could be used to simulate the compressibility effects of snow-covered surfaces, and Freon layers could be used to simulate density effects in boundary layers.

6. Hydrocode Simulations.

Inviscid hydrocode simulations of selected height-of-burst tests would be useful to examine the transition process for weak blast waves, and to completely eliminate wall boundary layer effects (e.g., by using an inviscid slip boundary condition on the surface). A second-order code with adaptive mesh refinement and front tracking is required for such studies.

7. Field Tests.

As already mentioned, the pressure waveforms are extremely peaked in the low-pressure transition region; this makes it difficult to accurately measure the peak pressure values in this region. In item 1 above, we recommended using the smaller-size PCB gauges to increase the temporal resolution of the pressure measurements in the 0.5-g charge height-of-burst tests. To increase the resolution even further, one must increase the scale of the explosion. For example, 0.5-kg charges (which could be used at the EMI test site at Wintersweiler) would increase the explosion scale by a factor of 10, and 8-lb charges (which could be

used at the DNA test site) would increase the explosion scale by a factor of 19. It would be useful to perform a few field tests with such larger charges and small PCB gauges — to check the waveforms and peak pressures in the transition region for burst heights around $1000 \text{ ft}/KT^{1/3}$.

SECTION 10 REFERENCES

- Ben Dor, G., and Glass, I.I. (1979) "Domains and boundaries of nonstationary oblique-shock reflections: 1 diatomic gas," *J. Fluid Mech.* **92**, pp. 459-496.
- Carpenter, H.J., and Brode, H. (1974), "Height-of-Burst Blast at High Overpressure," *Fourth Int. Symp. on Military Applications of Blast Simulations*, Southend-on-Sea, England.
- Carpenter, H.J., (1978) Letter to the Defense Nuclear Agency dated June 8, 1978.
- Colella, P. and Henderson, L.F. (1990) "The von-Neumann Paradox for the Diffraction of Weak Shock Waves," *J. Fluid Mechanics*, **213**, pp. 71-94.
- Ferguson, R. (1990), Private communication of an AMR calculation from NSW.
- Heilig, W., et al. (1985), *Ermittlung von HOB-Kurven und der Tripelpunktstrajektorien*, Bericht des Ernst-Mach Instituts, Freiburg, Germany, E 26/85.
- Heilig, W. (1990) "About the influence of the corner signal and the expansion wave in regular shock reflection processes," *9th Int. Mach Reflection Symposium*, Ernst-Mach-Institute, Freiburg, Germany.
- Kingery, C.N. and Bulmash, G. (1984), *Airblast Parameters from TNT Spherical Air Burst and Hemispherical Burst*, Techn. Rep. ARBRL-TR-02555.
- Lock, G.D. and Dewey, J.M. (1989) "An experimental investigation of the sonic criterion for transition from regular to Mach reflection of weak shock waves," *Experiments in Fluids*, **7**, pp. 289-292.
- Petes, J. (1986), *Handbook of High Explosions Effects*, DASIAC Report TN-86-15.
- Reichenbach, H. and Kuhl, A.K. (1989), "HOB Experiments with 0.5-g Charges," *Eleventh Int. Symp. on Military Applications of Blast Simulations*, Albuquerque, NM, pp. 597-611.
- Reisler, R. et al. (1988), *DIAMOND ARC87 - Blast Phenomenology Results from HOB, HE Tests with a Helium Layer*, DNA-TR-87-99-V2-AP-A-G.
- Sauer, F.M. (1990) Letter to the Defense Nuclear agency dated August 14, 1990.

- Scheklinski-Glück, G. and Reichenbach, H. (1990), *Analysis of Pressure Data from Height-of-Burst Tests with RDX Charges*, Ernst-Mach-Institut, Freiburg, Germany, Report T 2/90.
- Sedov, L.I. (1959), *Similarity and Dimensional Methods in Mechanics*, Academic Press, N.Y.
- Smiley, R.F., Reutenik, J.R. and Tomayko (1981) *REFLECT-4 Code Computations of 40-KT Nuclear Blast Waves Reflected from the Ground*, DNA-TR-81-203, Vol. 1: General Results, Vol. 2: Detailed Data and Plots. (also see DNA-TR-84-178 Volumes 1-3 and DNA-TR-84-348 Volumes 1 and 2).
- Wisotski, J. (1990) "Reflection coefficients from natural and artificial surfaces," *9th Mach Reflection Symposium*, Ernst-Mach-Institut, Freiburg, Germany.

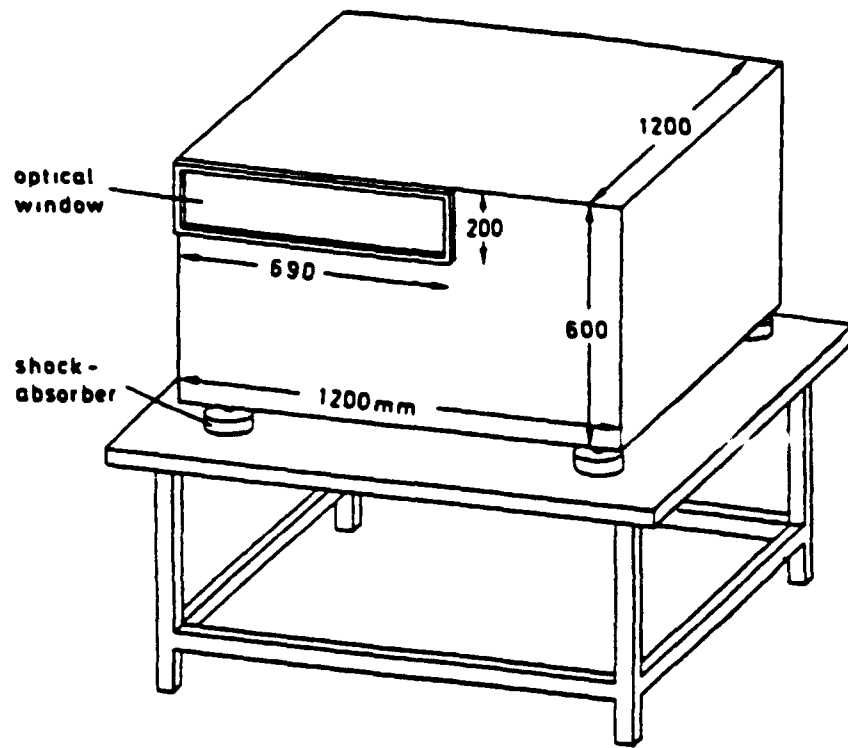


Figure 1. Schematic of the explosion chamber.

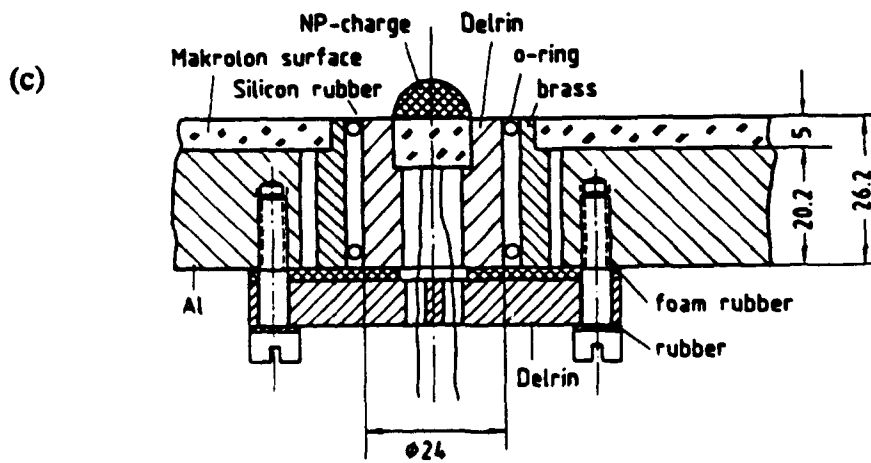
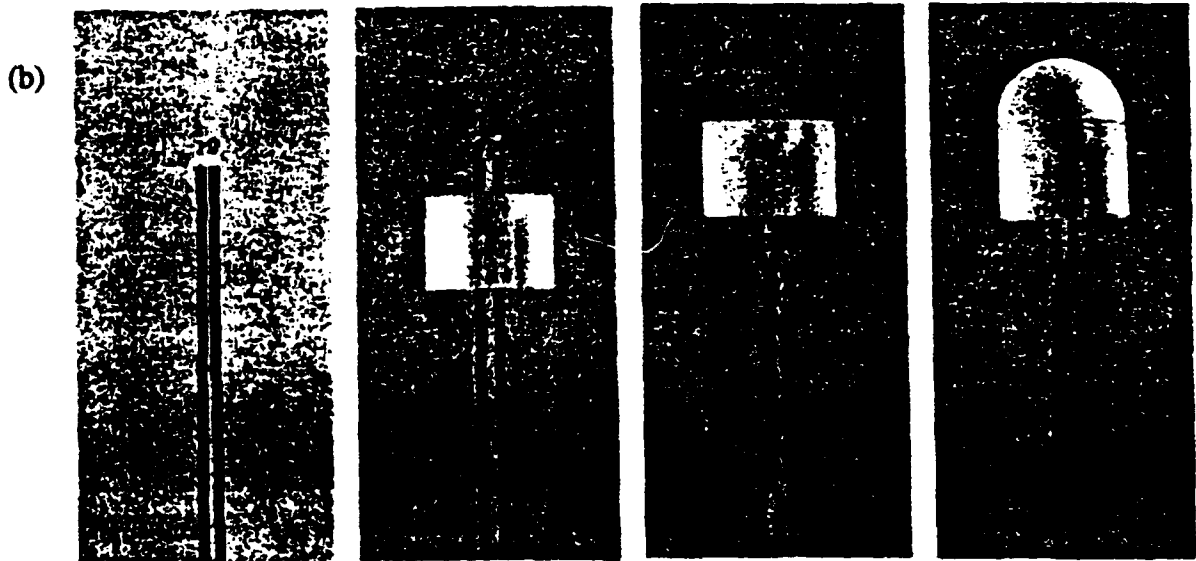
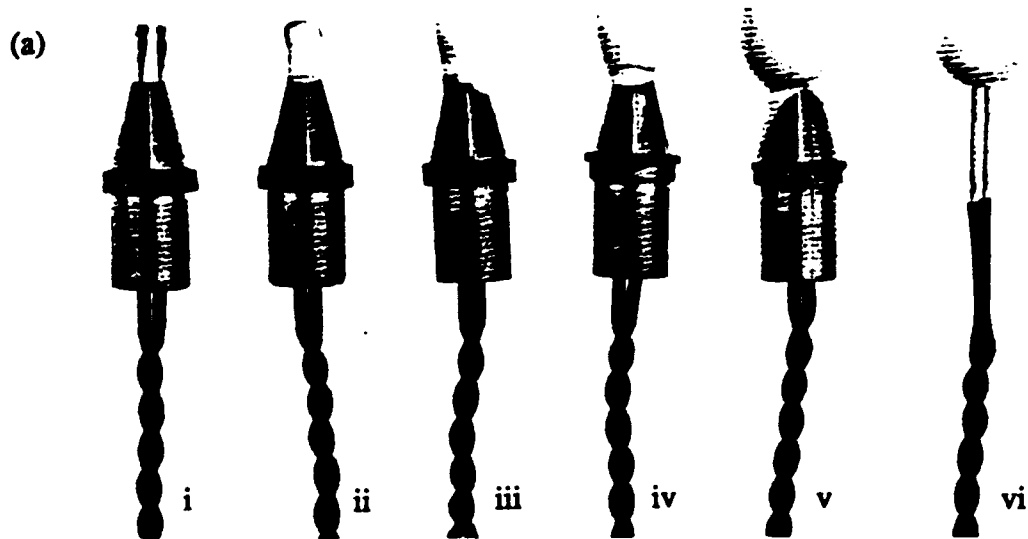


Figure 2. Construction of NP charges: (a) spherical charge; (b) hemispherical charge; (c) mounting bracket for the hemispherical charge.

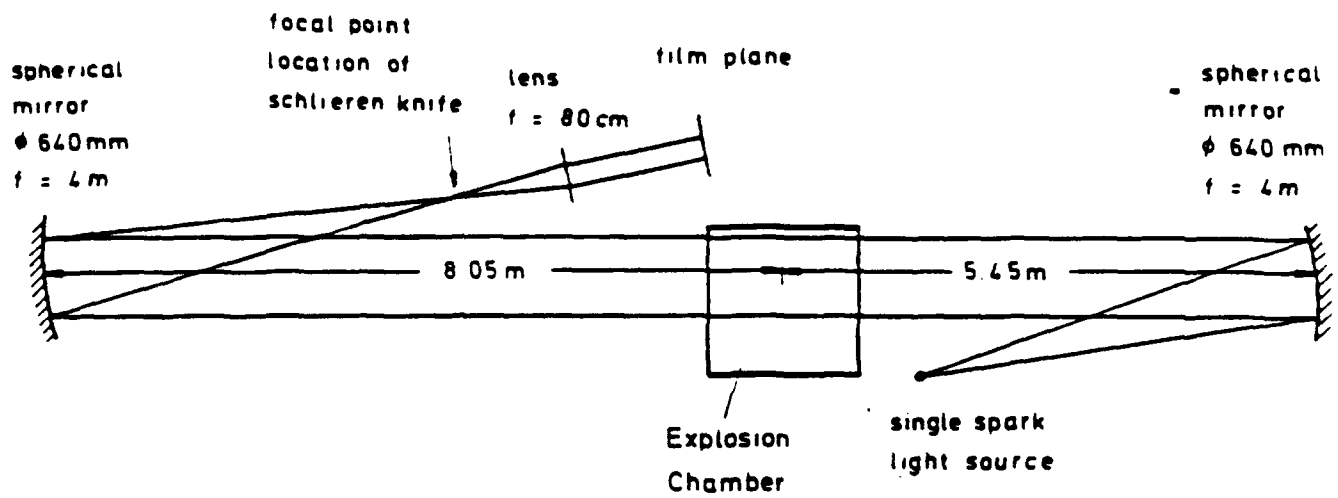


Figure 3. Schematic of the photography system.

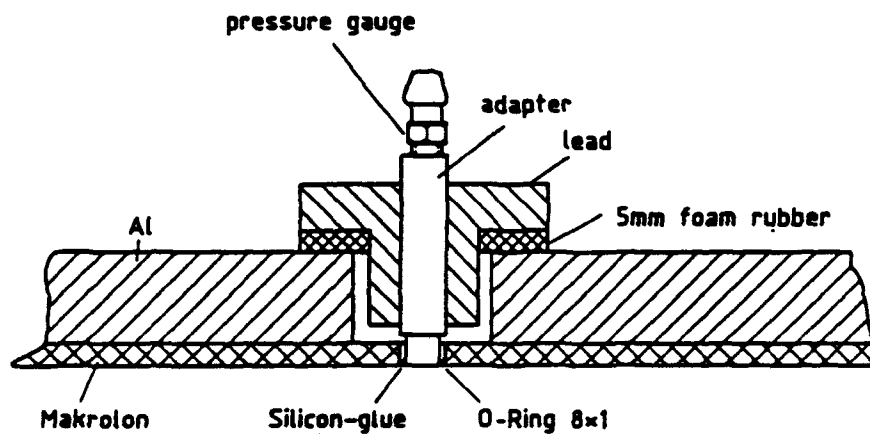


Figure 4. Schematic of the pressure gauge mount.

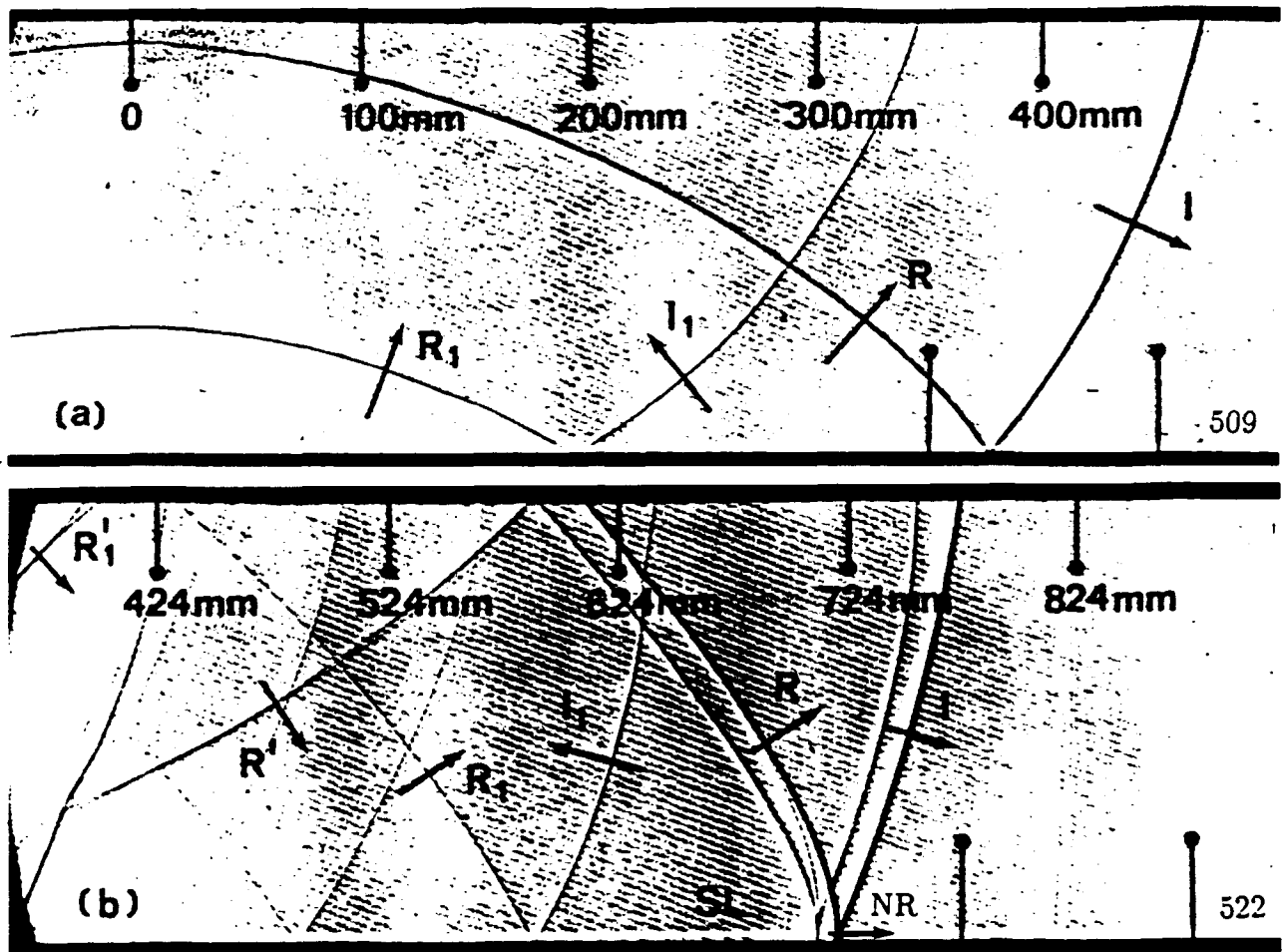


Figure 5. Shadow photographs showing the blast reflection over the Makrolon surface for HOB = 303 mm = $3.8 \text{ m/kg}^{1/3}$: (a) regular reflection structure near transition ($GR = 4.73 \text{ m/kg}^{1/3}$, $\alpha = 51.2^\circ$, $\Delta p_I = 4.1 \text{ psi}$ and $\Delta p_R \approx 10 \text{ psi}$); (b) Neumann reflection shock structure well past transition ($GR = 9.02 \text{ m/kg}^{1/3}$, $\alpha = 67^\circ$, $\Delta p_I = 2 \text{ psi}$ and $\Delta p_R \approx 5 \text{ psi}$).

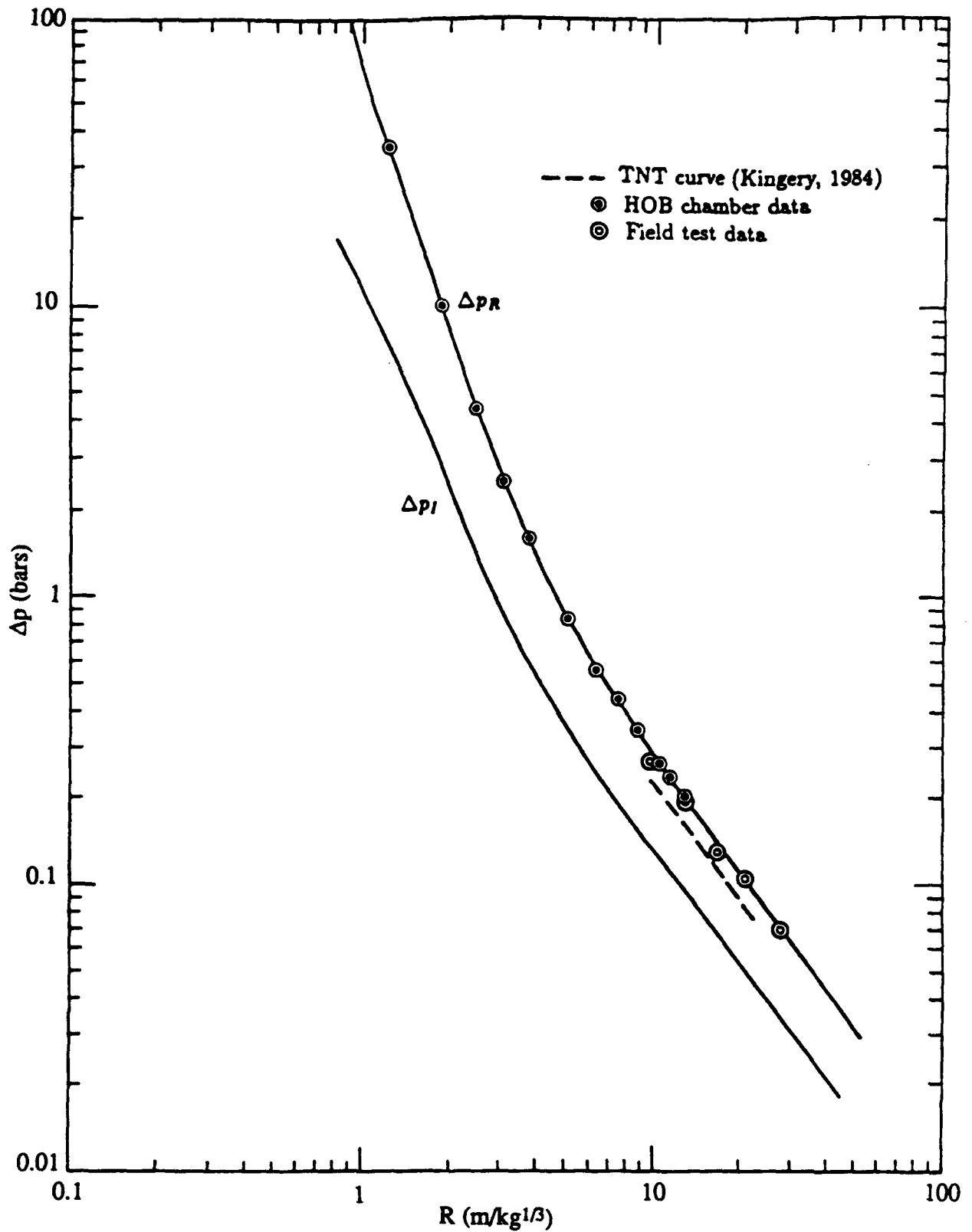


Figure 6. Pressure-range curves for 0.5-g NP charges (subscripts *I* and *R* denote incident and reflected values, respectively).

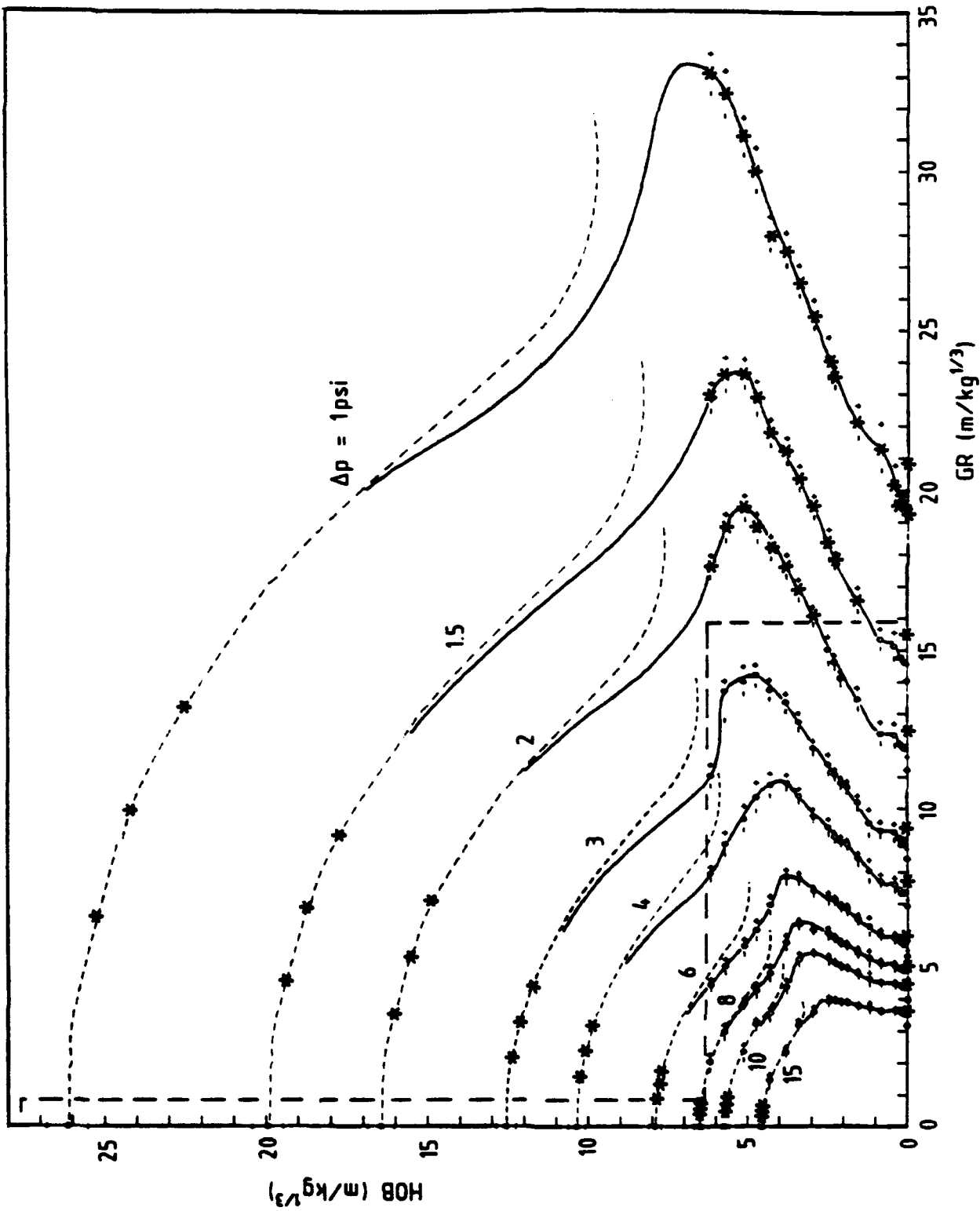


Figure 7. Peak-pressure height-of-burst curves for a hydrodynamically-smooth surface in the low-pressure regime: circles denote mean values, $\pm 1\sigma$ uncertainty bands, stars denote extrapolated points.

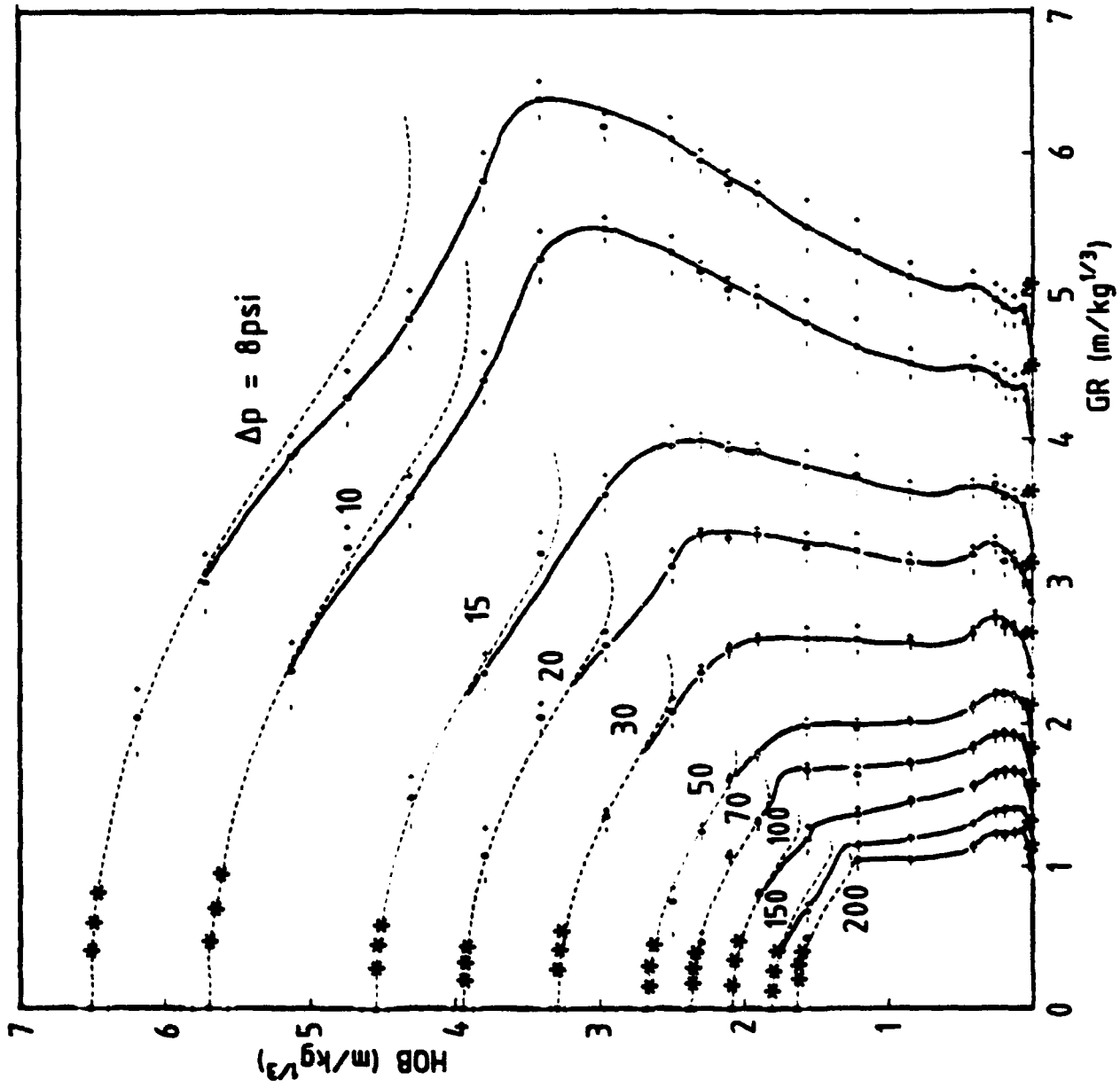


Figure 8. Peak-pressure height-of-burst curves for a hydrodynamically-smooth surface in the intermediate-pressure regime: notation is the same as Figure 7.

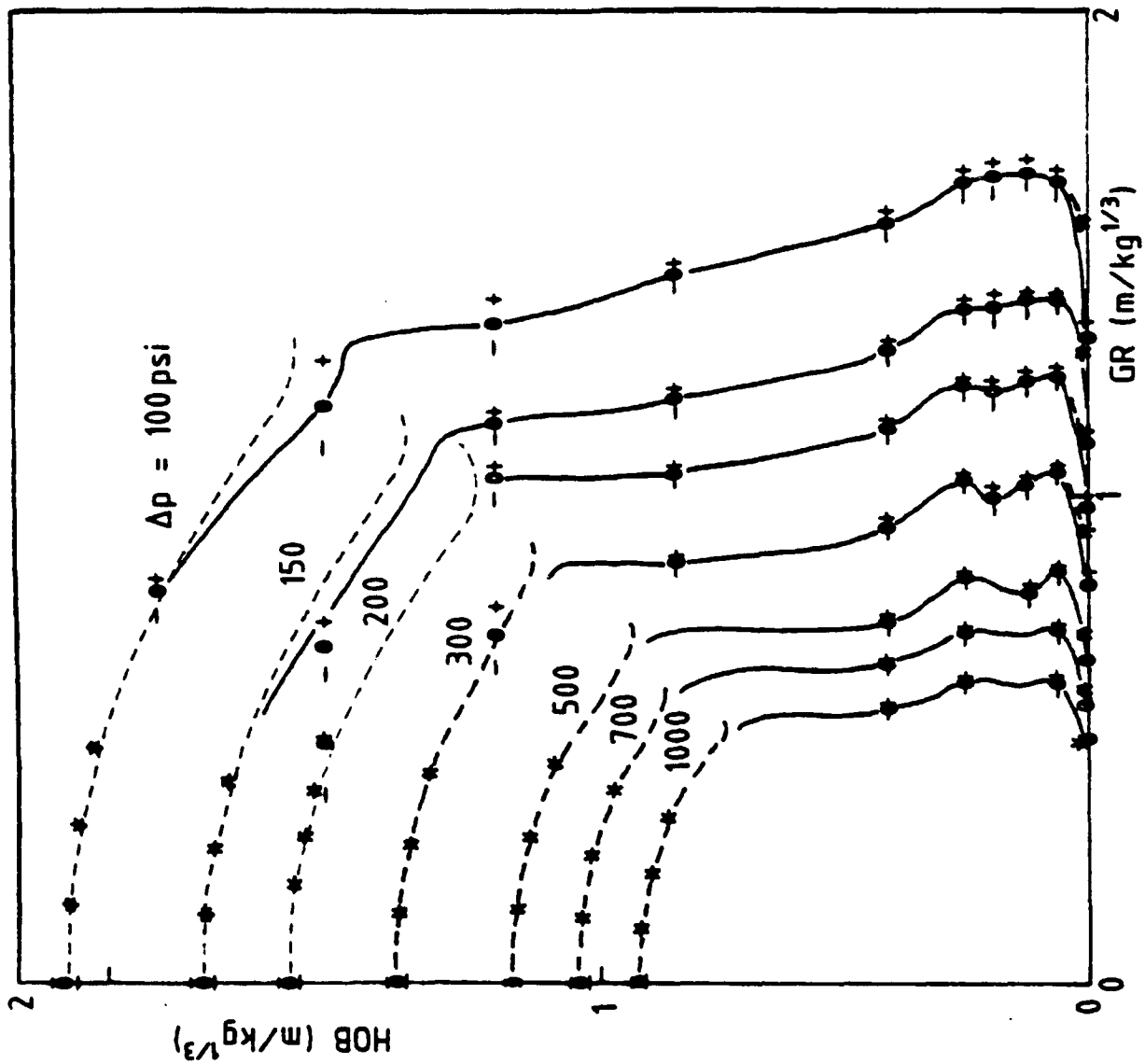


Figure 9. Peak-pressure height-of-burst curves for a hydrodynamically-smooth surface in the high-pressure regime: notation is the same as Figure 7.

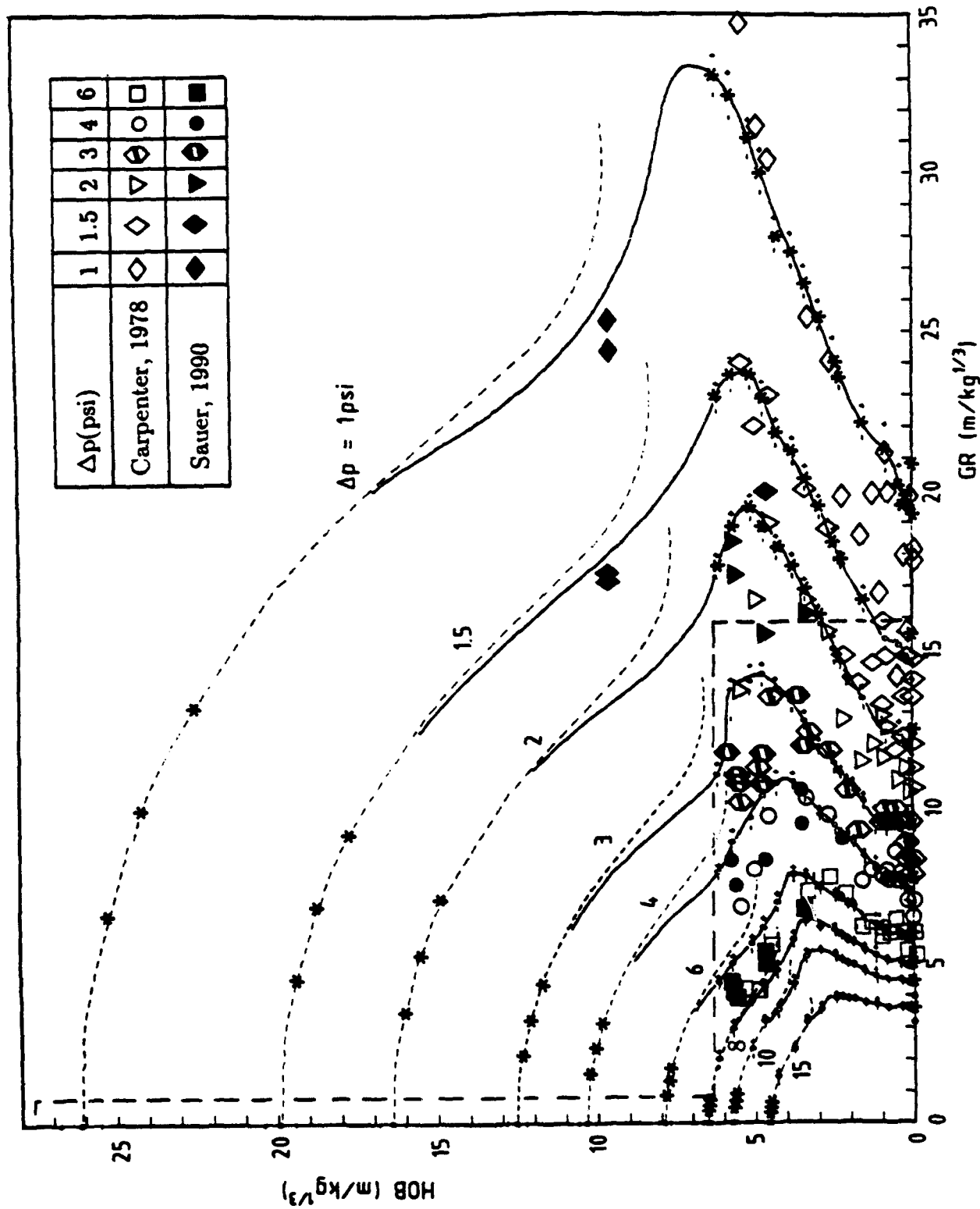


Figure 10. Comparison of the NP height-of-burst curves for a smooth surface with data from 450-kg TNT charges ($\Delta p = 1$ to 15 psi).

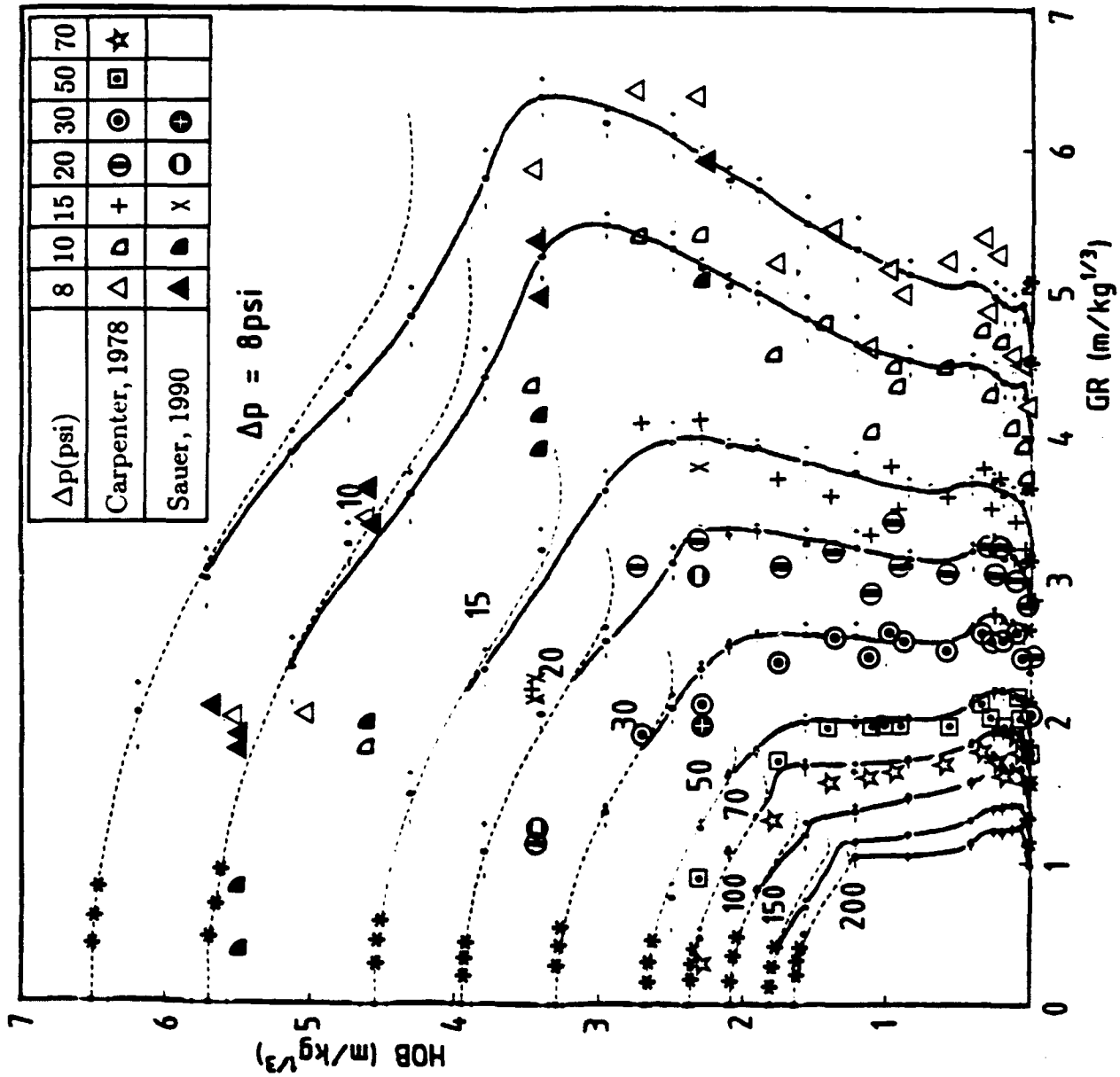


Figure 11. Comparison of the NP height-of-burst curves for a smooth surface with data from 450-kg TNT charges ($\Delta p = 8$ to 200 psi).

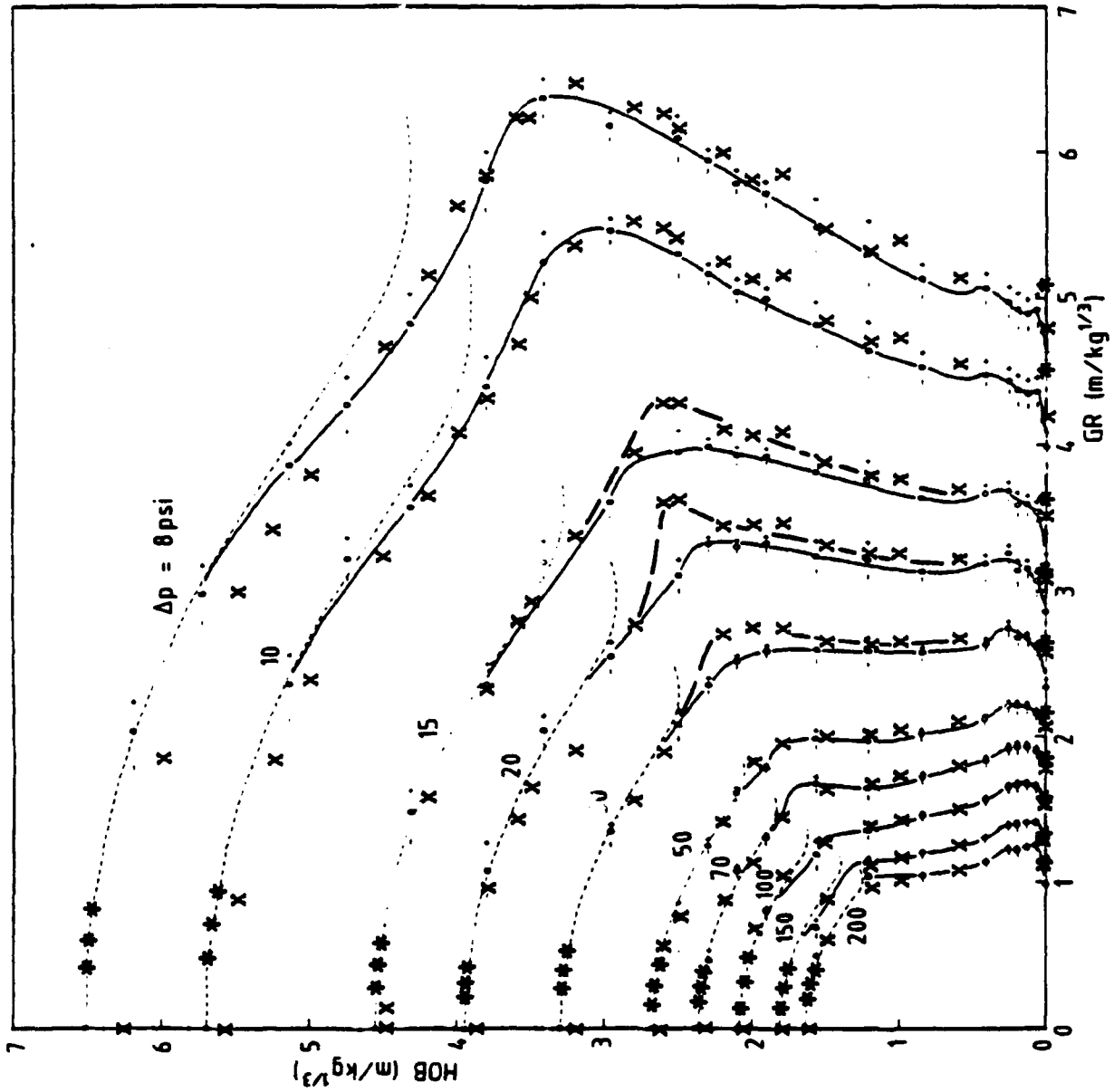


Figure 12. Comparison of the NP height-of-burst curves for a smooth surface with data from 1-kg RDX charges (symbol x).

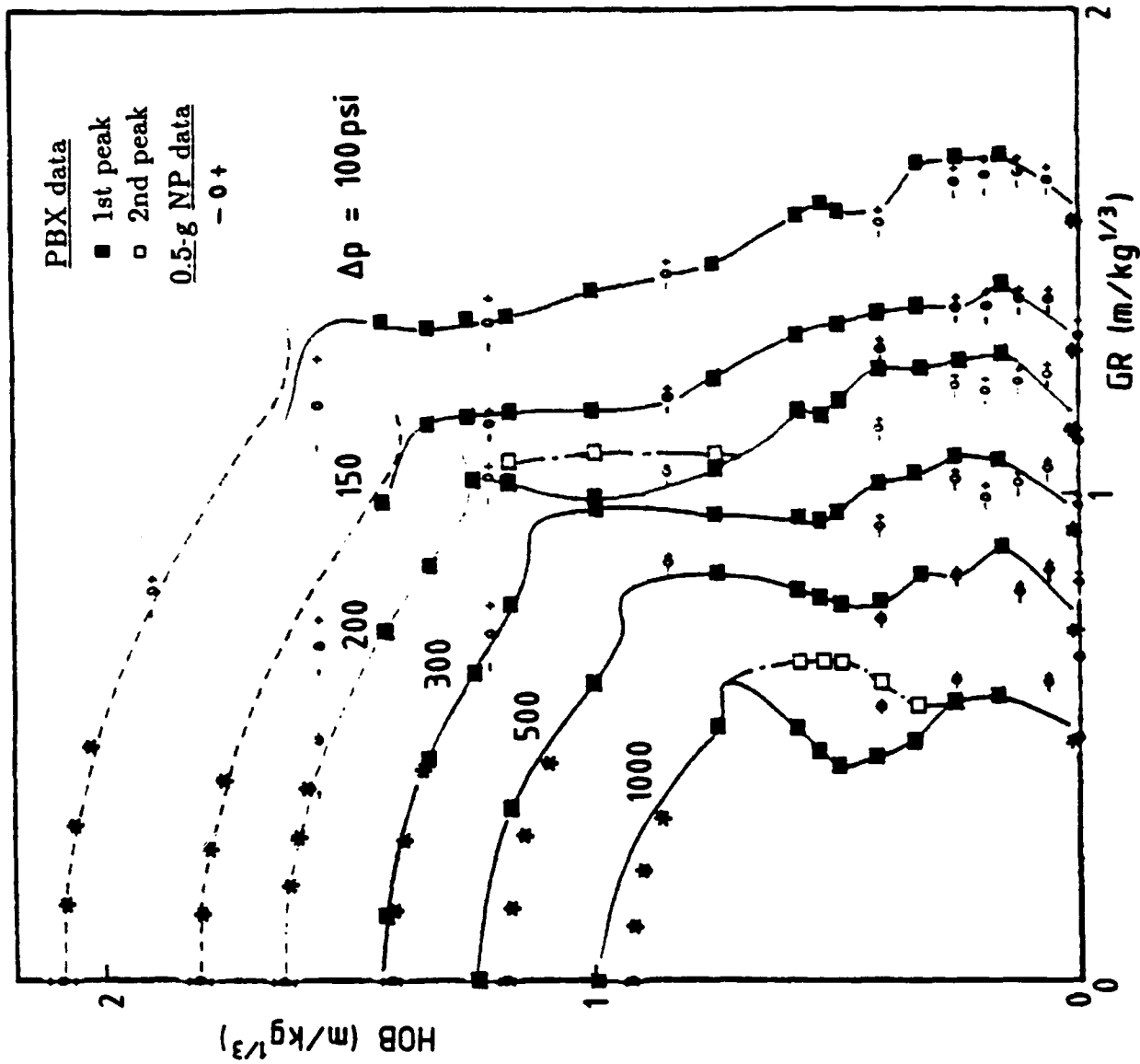


Figure 13. Comparison of the NP data with the height-of-burst curves for 3.6-kg PBX-9404 charges (Carpenter and Brode, 1974).

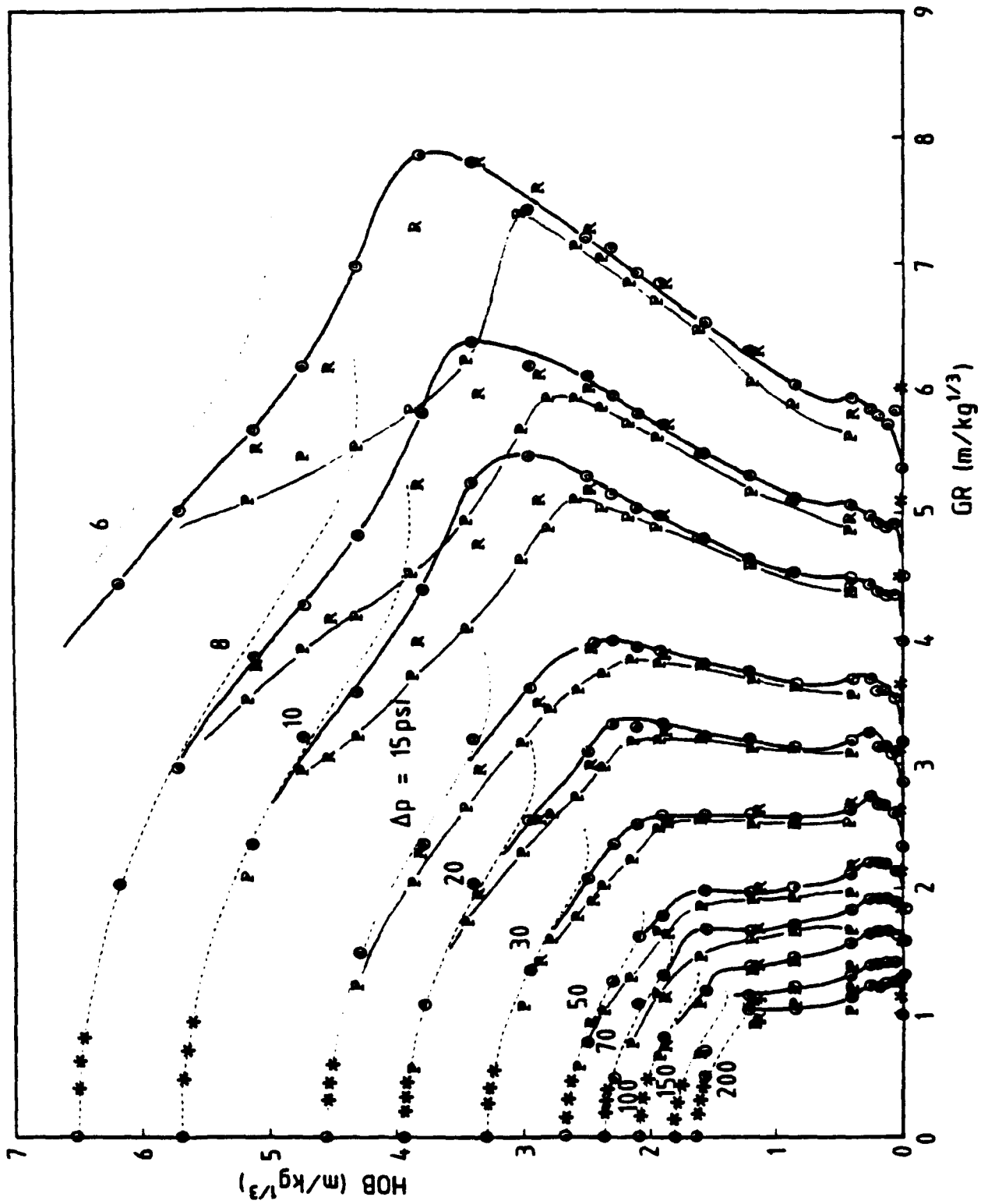


Figure 14. Peak-pressure height-of-burst curves for a smooth surface (symbol O), a rough surface (symbol R) and a porous surface (symbol P).

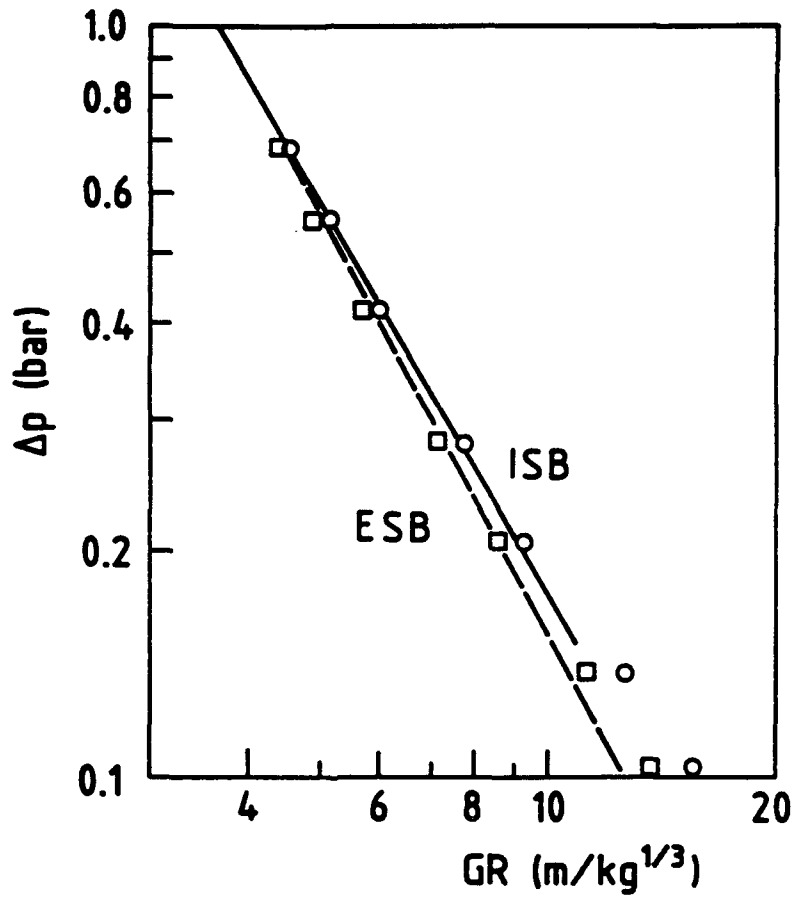


Figure 15. Peak-pressure decay with range for surface bursts: circles denote an ideal surface; squares denote an extrapolated surface burst.

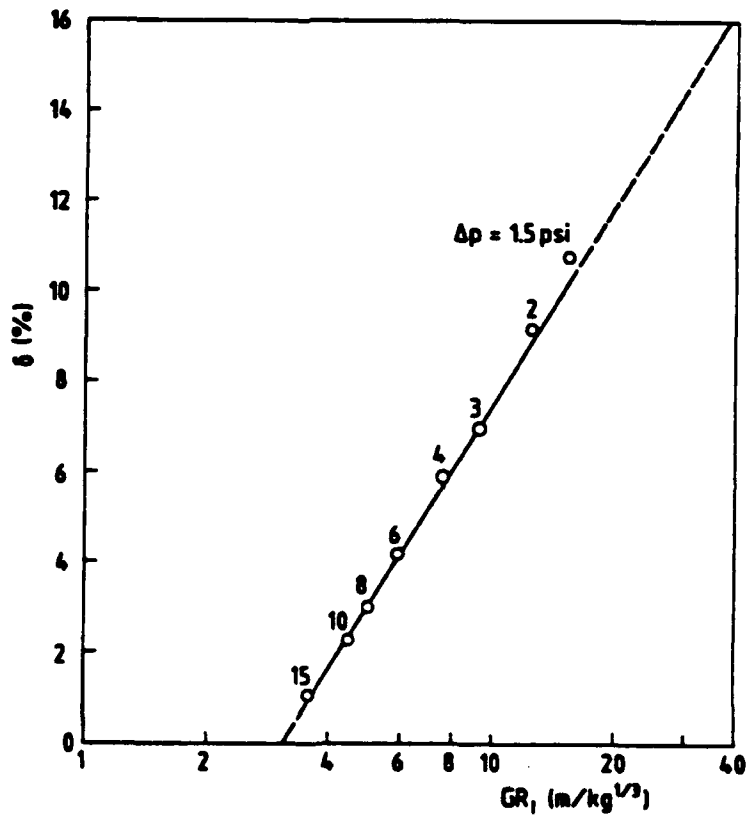


Figure 16. Ground range decrement, δ , versus ideal range.

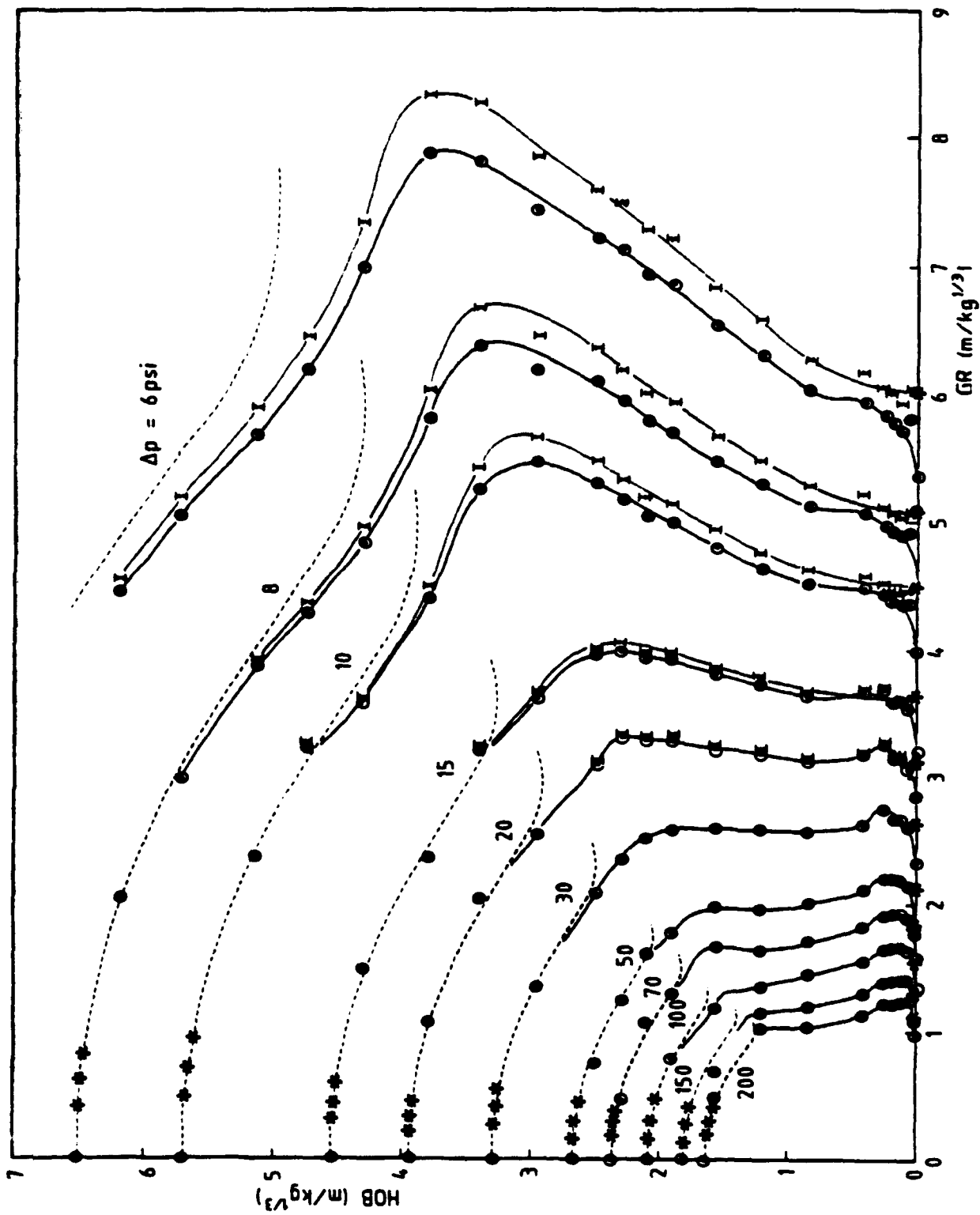


Figure 17. Peak-pressure height-of-burst curves for a smooth surface (symbol O) and an ideal surface (symbol I) in the intermediate-pressure regime.

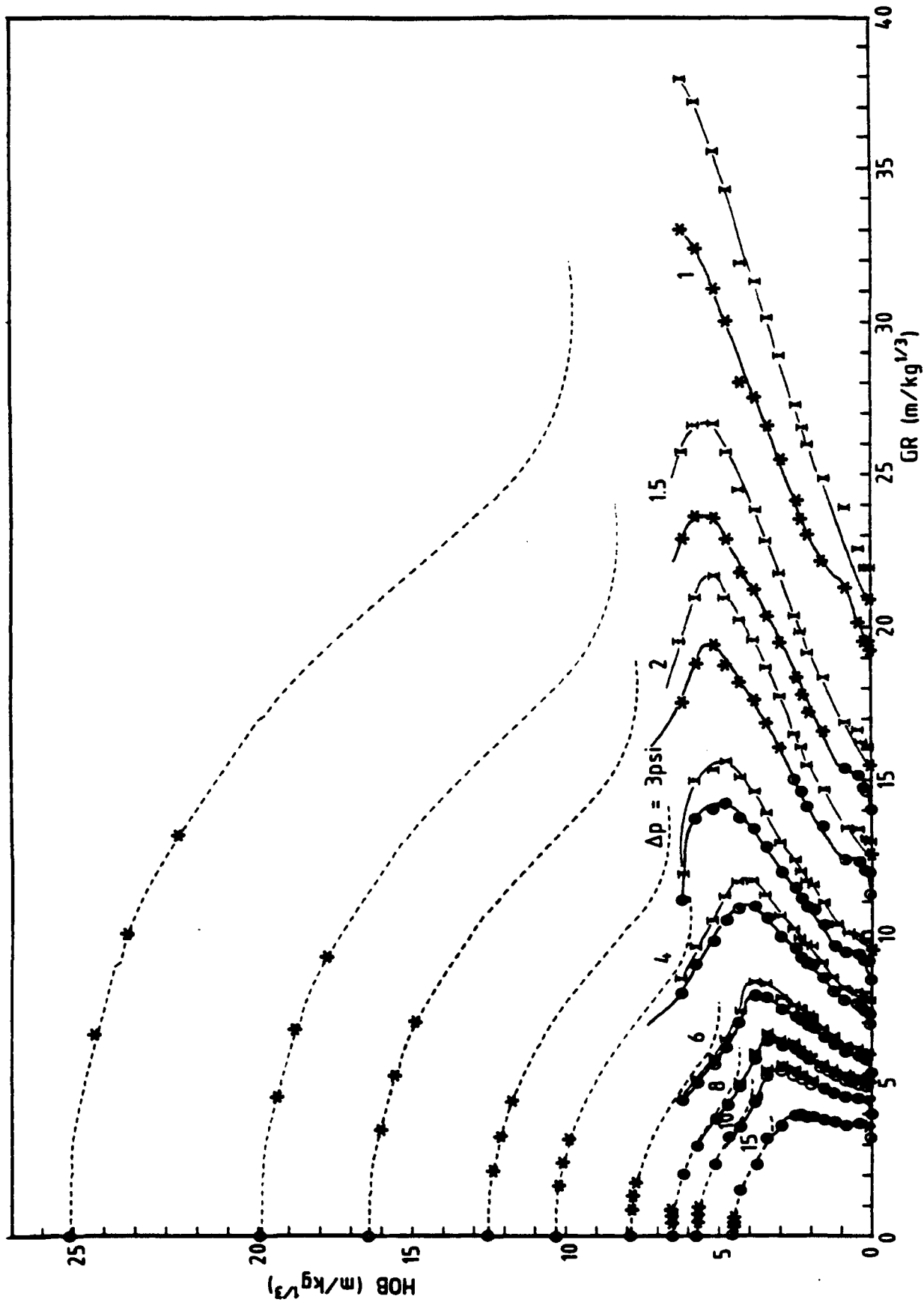


Figure 18. Peak-pressure height-of-burst curves for a smooth surface (symbol *O*) and an ideal surface (symbol *I*) in the low-pressure regime. The curves for $\Delta p = 2, 1.5$ and 1 psi are extrapolated.

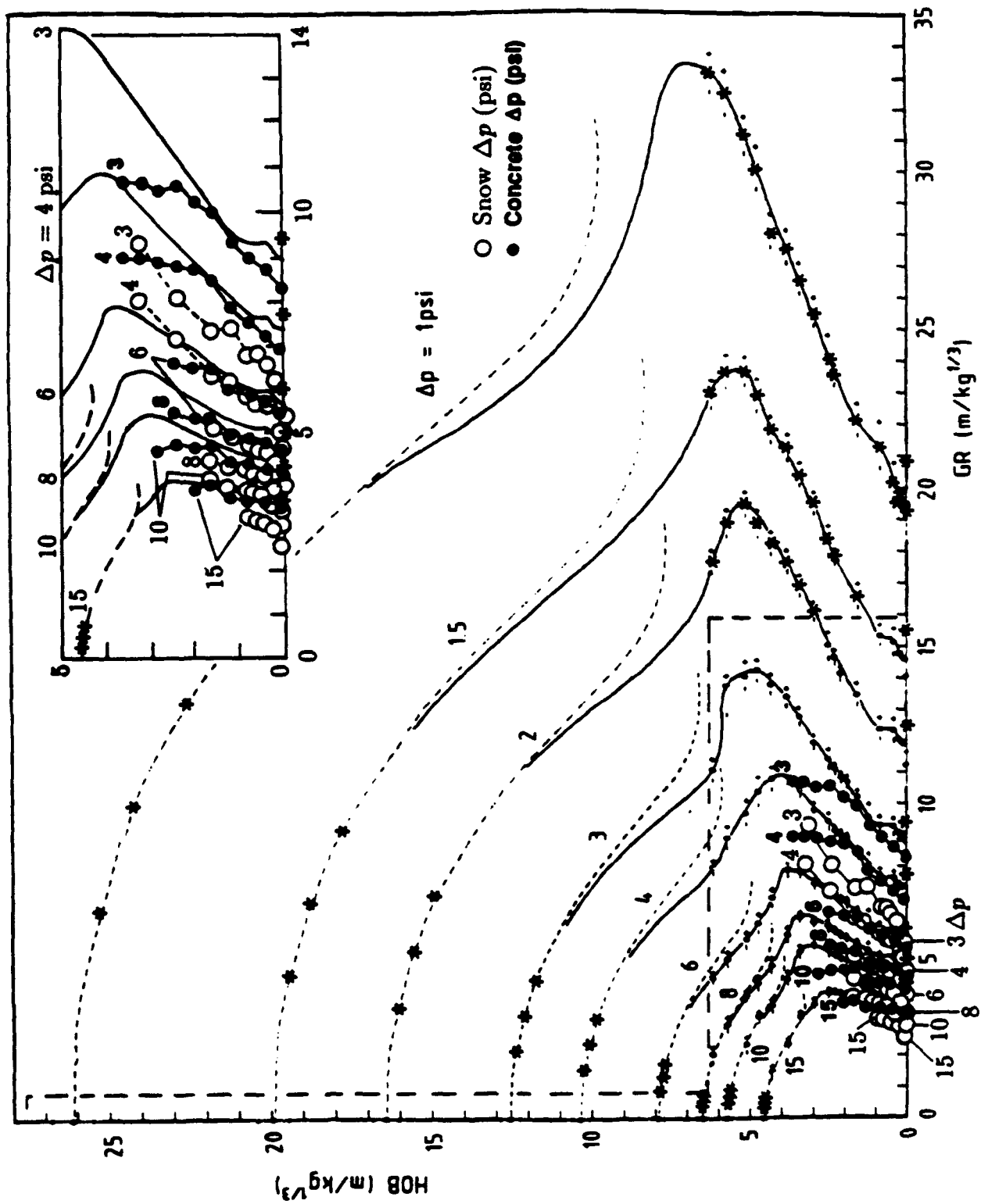


Figure 19. Comparison of reflected pressures on a deep snow surface (Wisotski, 1990) with the smooth-surface NP results (low-pressure regime).

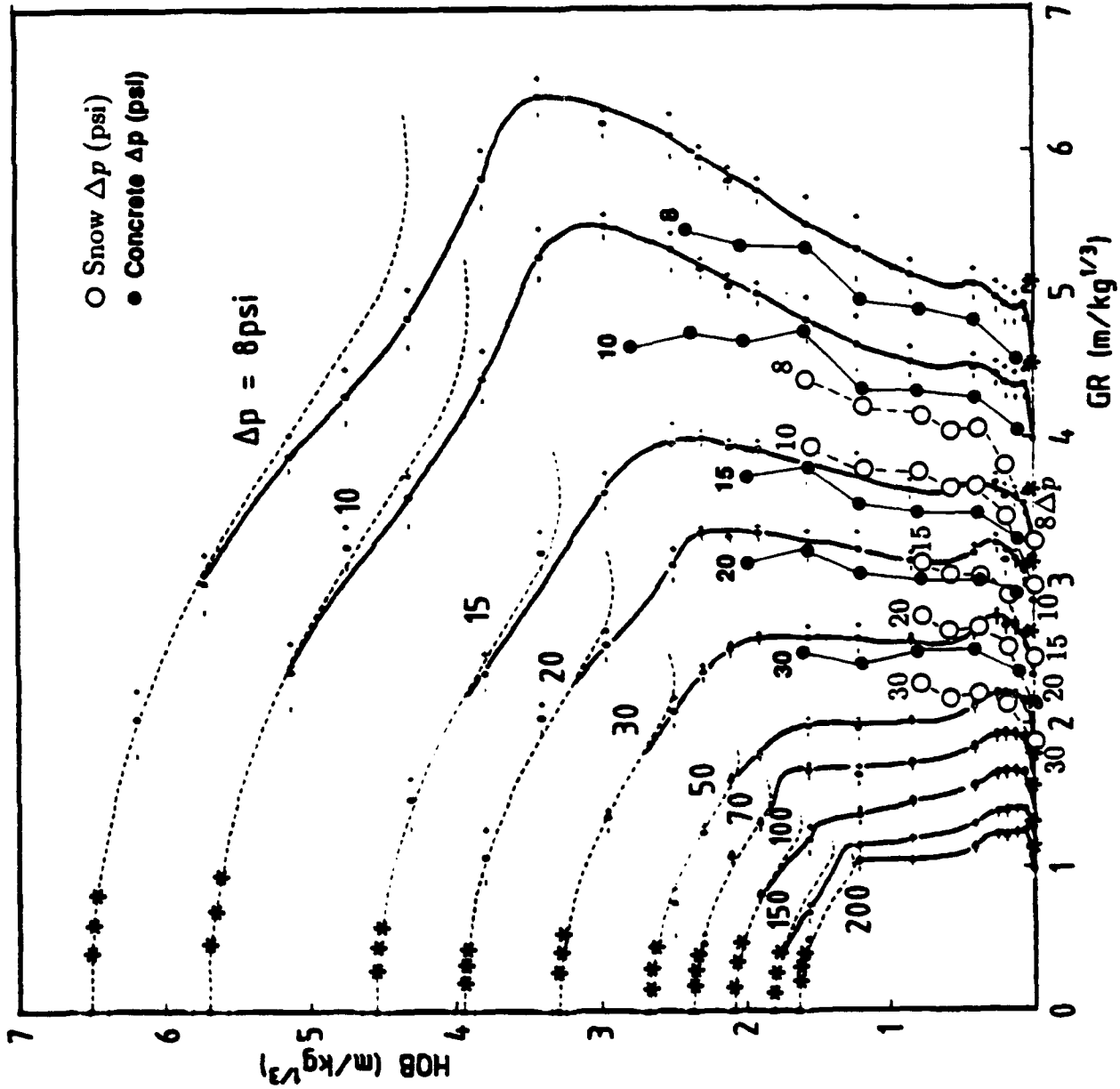


Figure 20. Comparison of reflected pressures on a deep snow surface (Wisotski, 1990) with the smooth-surface NP results (intermediate-pressure regime).

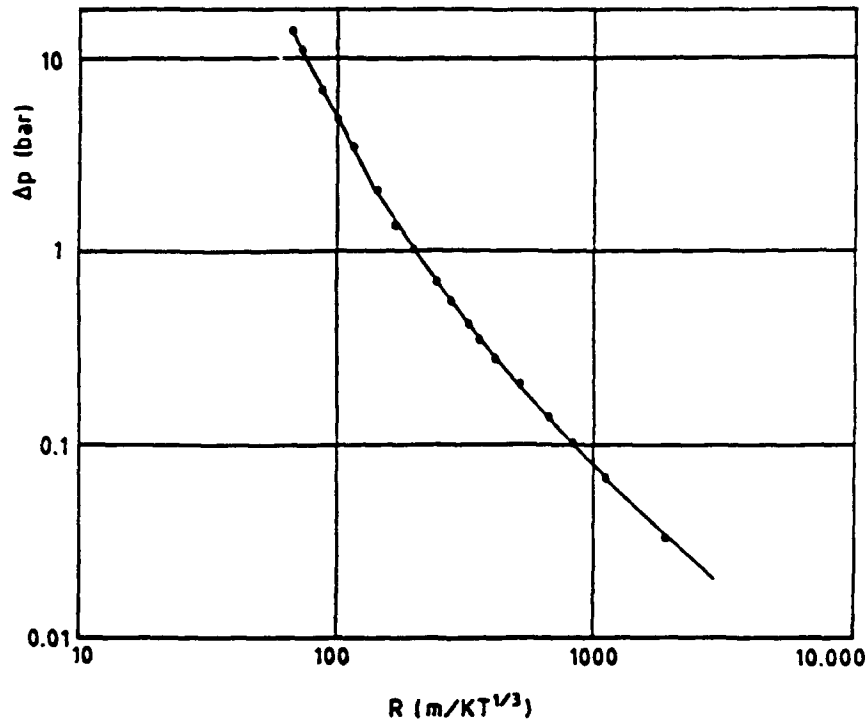


Figure 21. Free-air peak pressure versus radius curve for point-source explosions (Smiley et al., 1981). Circles denote the NP free-air data points scaled by function SF.

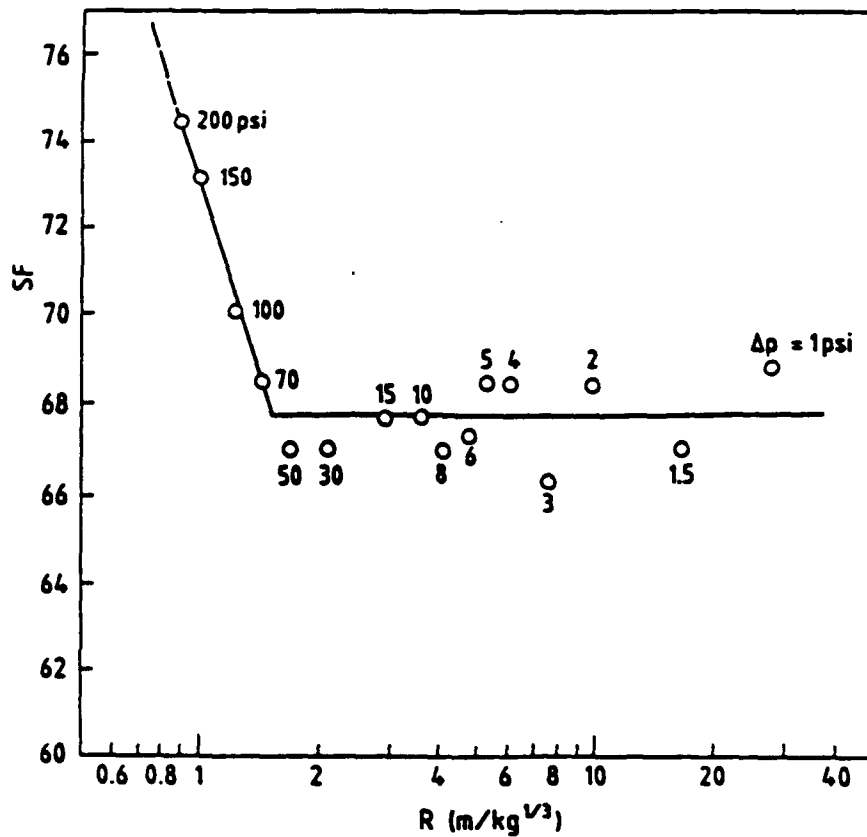


Figure 22. Scale function, $SF = R_n/R_{NP}$, versus shock radius, R_{NP} , for NP charges.

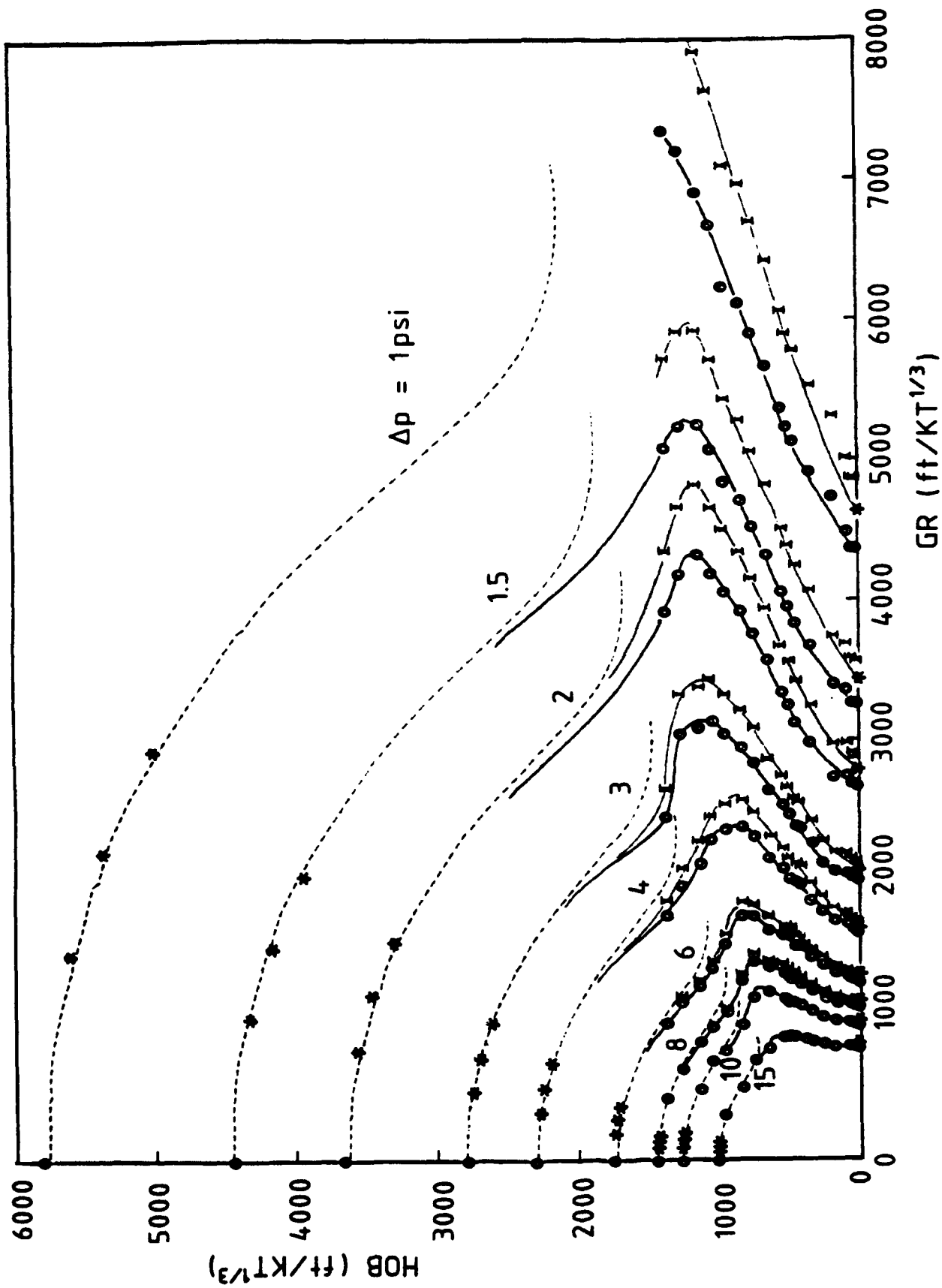


Figure 23. NP height-of-burst curves for a smooth surface (symbol O) and an ideal surface (symbol I) scaled to a 1-KT point explosion by function SF for $\Delta p = 1$ to 15 psi.

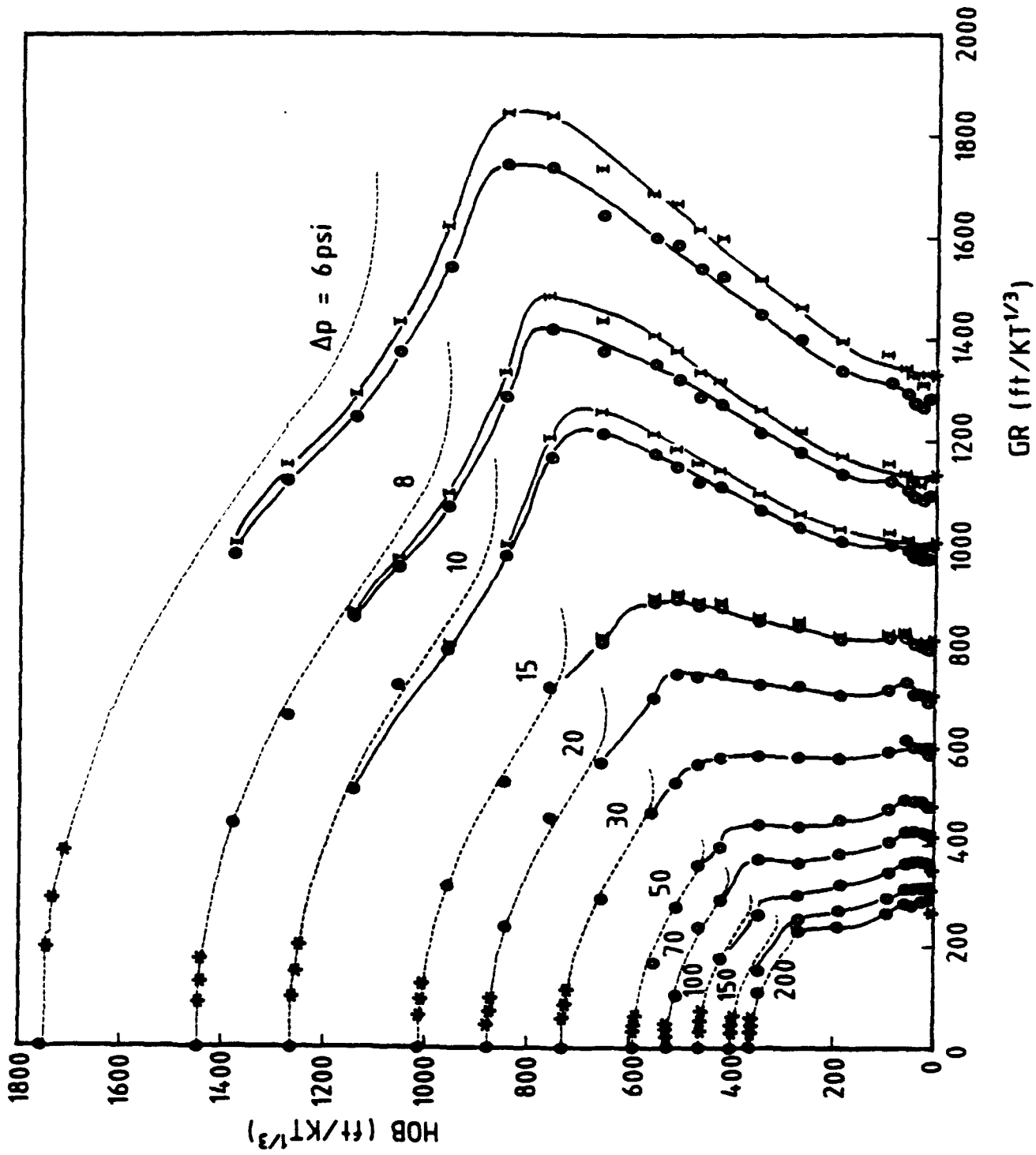


Figure 24. NP height-of-burst curves for a smooth surface (symbol O) and an ideal surface (symbol I) scaled to a 1-KT point explosion by function SF for $\Delta p = 6$ to 200 psi.

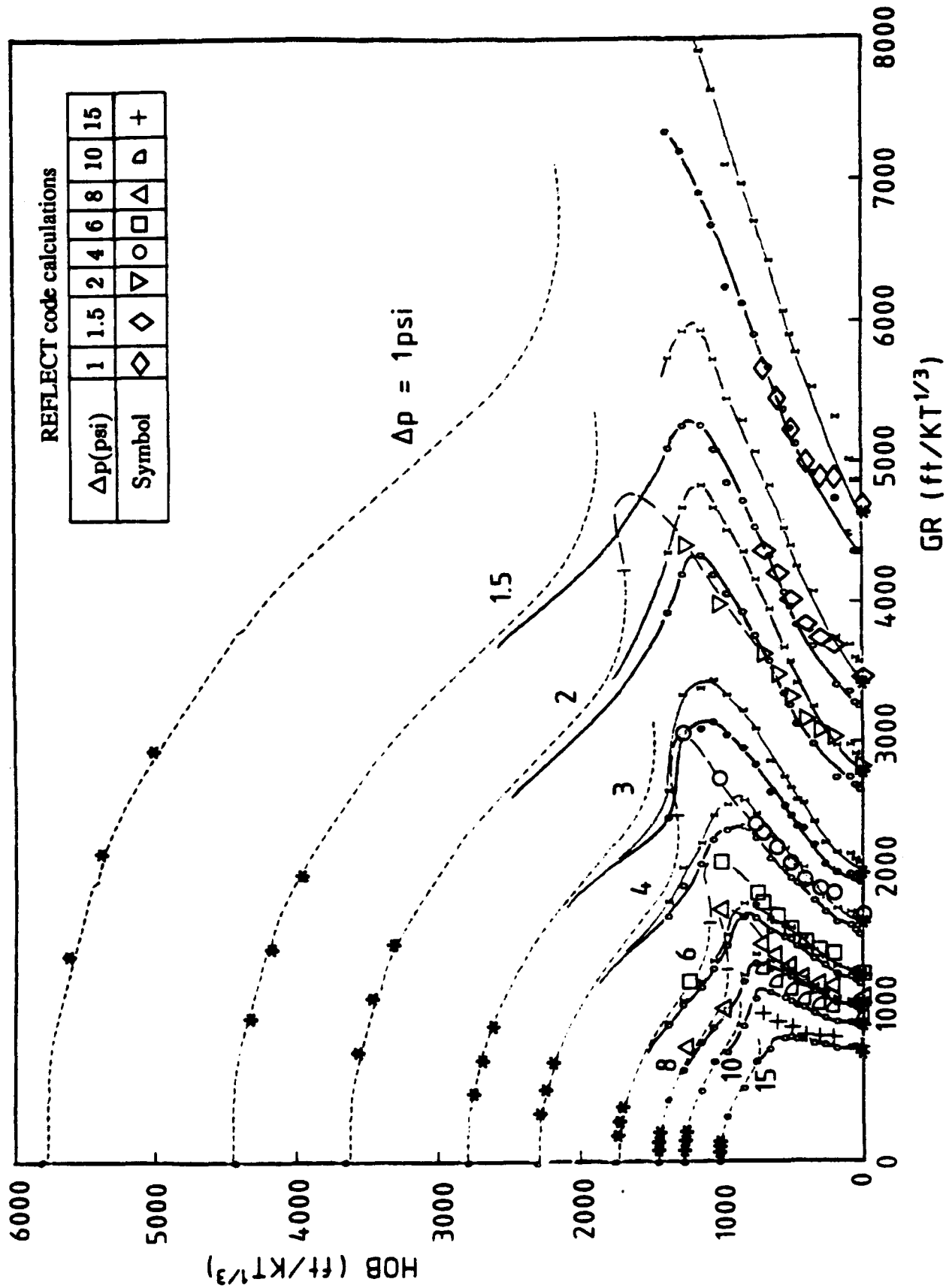


Figure 25. Comparison of the scaled NP height-of-burst curves with REFLECT code calculations of point explosions (Smiley et al., 1981) for $\Delta p = 1$ to 15 psi.

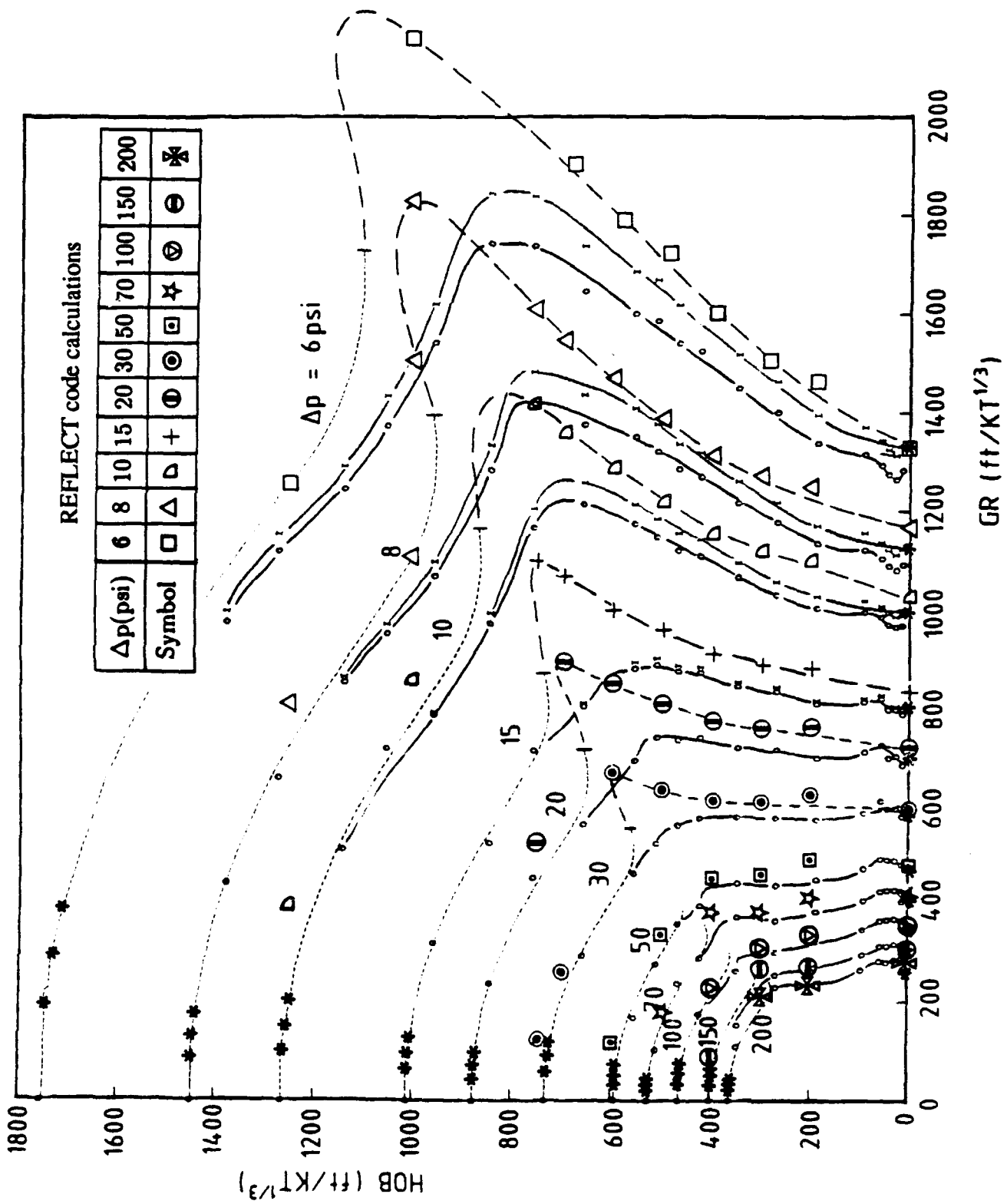


Figure 26. Comparison of the scaled NP height-of-burst curves with REFLECT code calculations of point explosions (Smiley et al., 1981) for $\Delta p = 6$ to 200 psi.

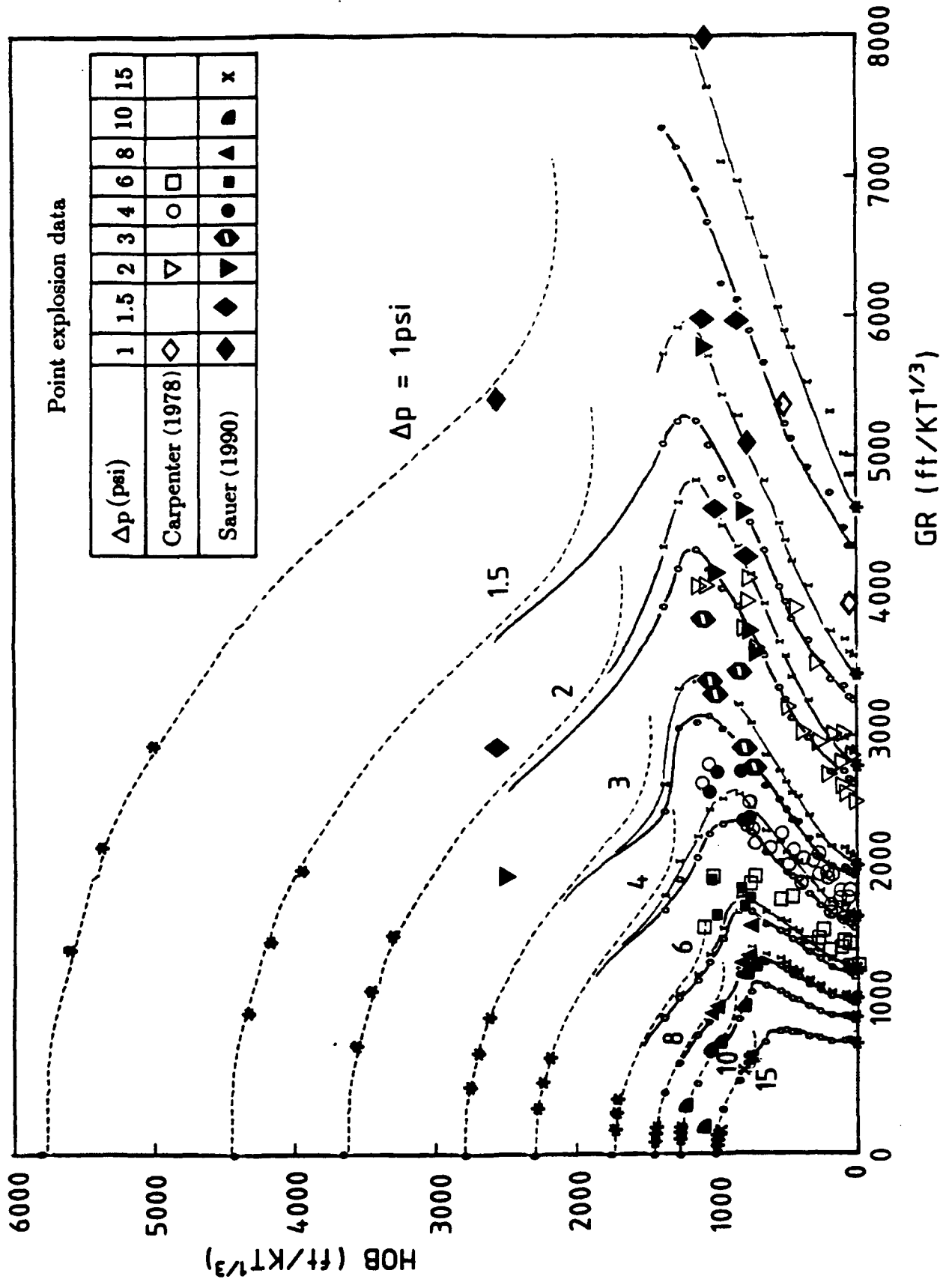


Figure 27. Comparison of the scaled NP height-of-burst curves with point explosion data, $\Delta p = 1$ to 15 psi.

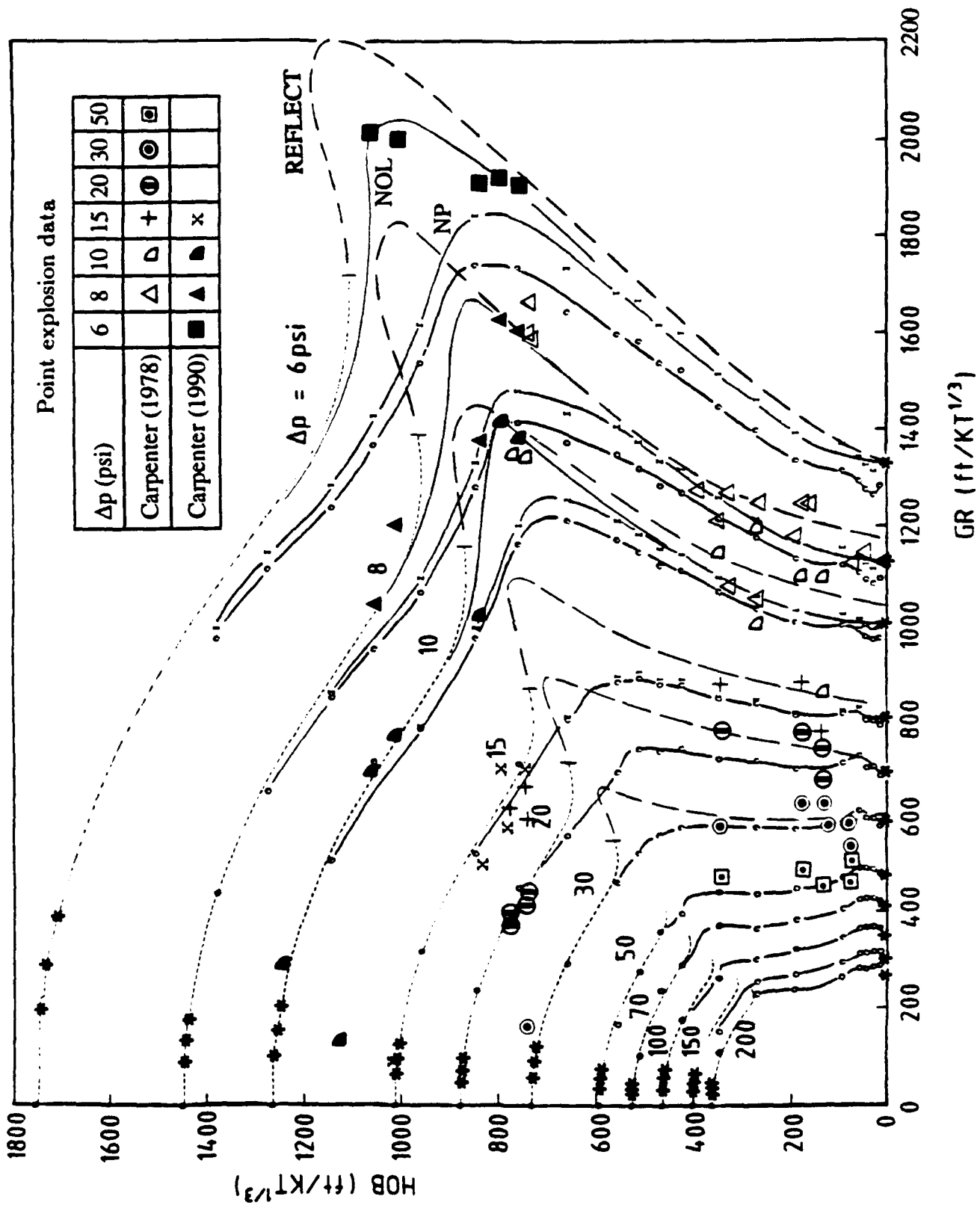


Figure 28. Comparison of the scaled NP height-of-burst curves with point explosion data, Δp = 6 to 200 psi.

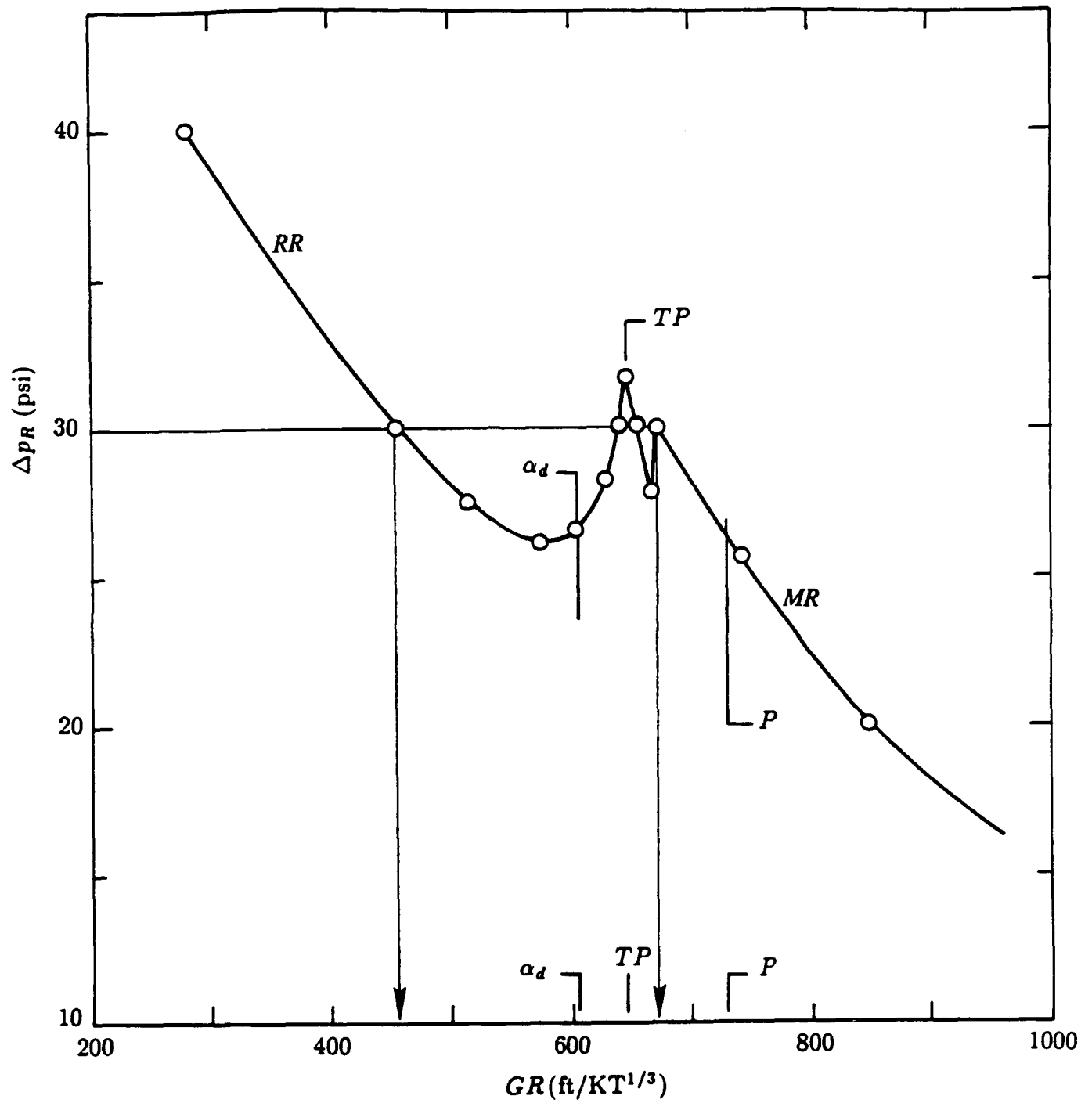


Figure 29. Peak pressure vs. range for a point explosion at $HOB = 600 \text{ ft}/KT^{1/3}$ from the REFLECT code calculations (Smiley et al., 1981).

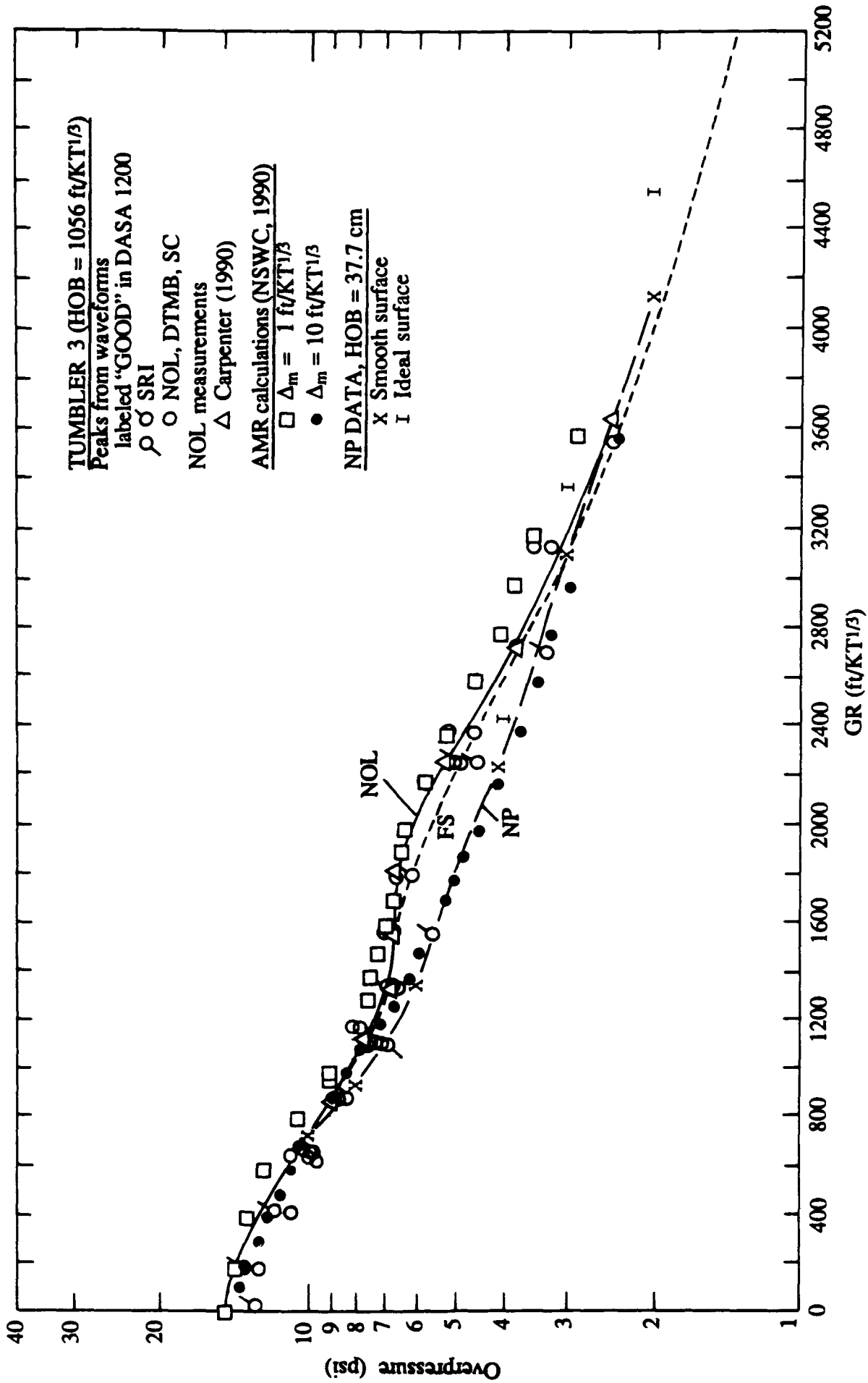


Figure 30. Comparison of peak-overpressure vs. range curves for HOB = 1056 ft/KT^{1/3}.

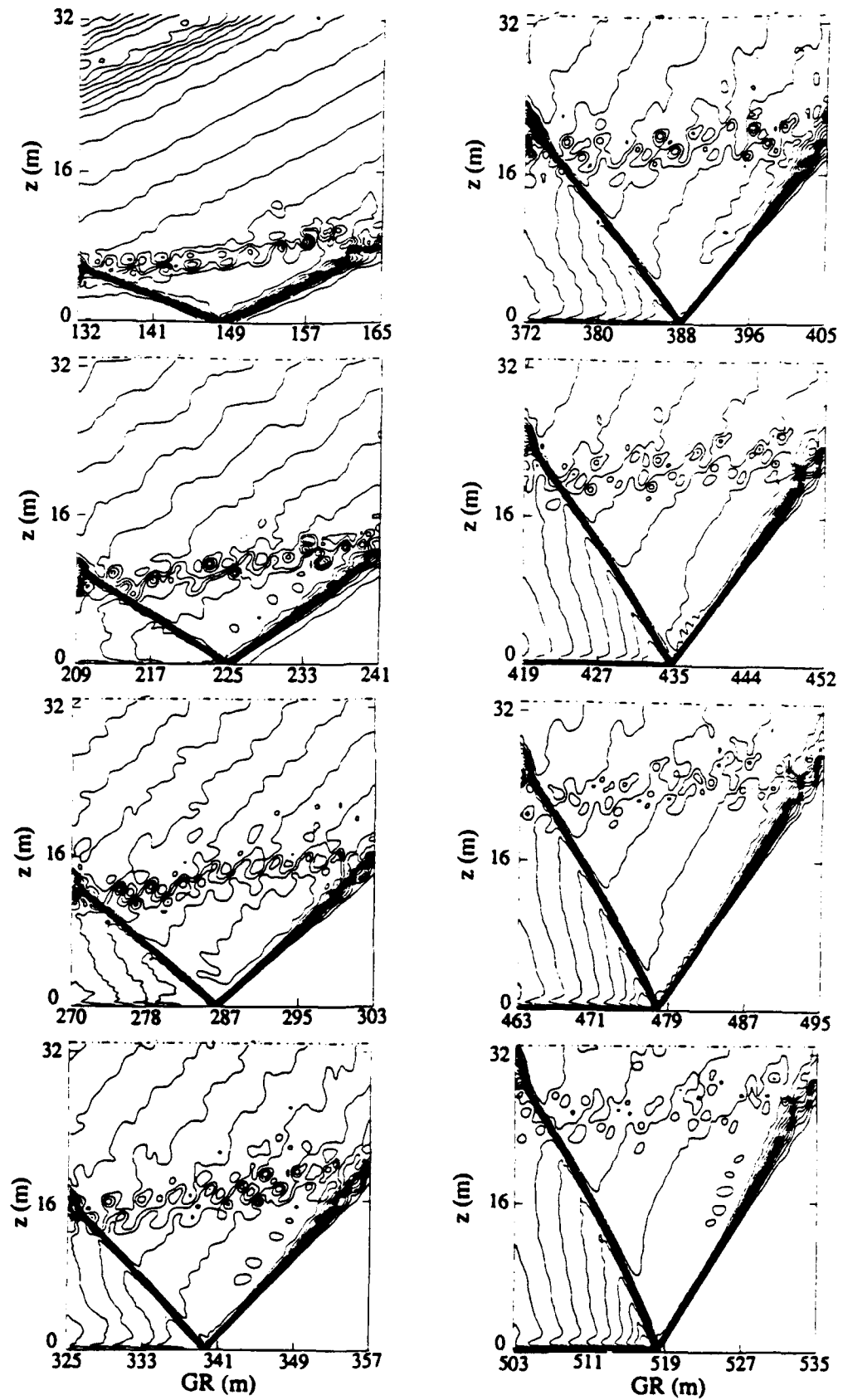


Figure 31. Entropy contours showing the reflection of a point-source blast wave from a plane; $HOB = 1056/KT^{1/3} = 322 \text{ m}/KT^{1/3}$.

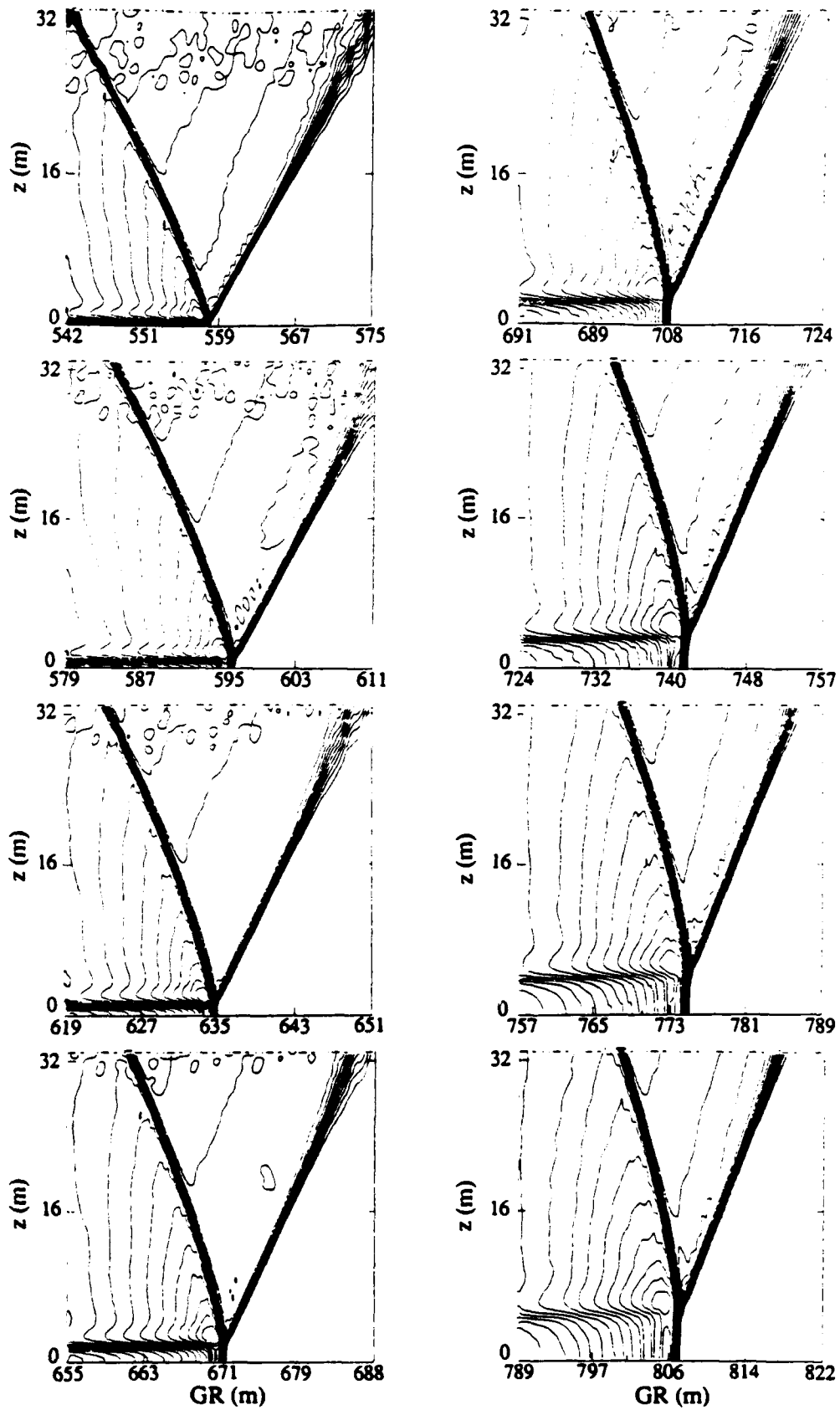


Figure 31. Entropy contours showing the reflection of a point-source blast wave from a plane; $HOB = 1056/KT^{1/3} = 322 \text{ m}/KT^{1/3}$ (Continued).

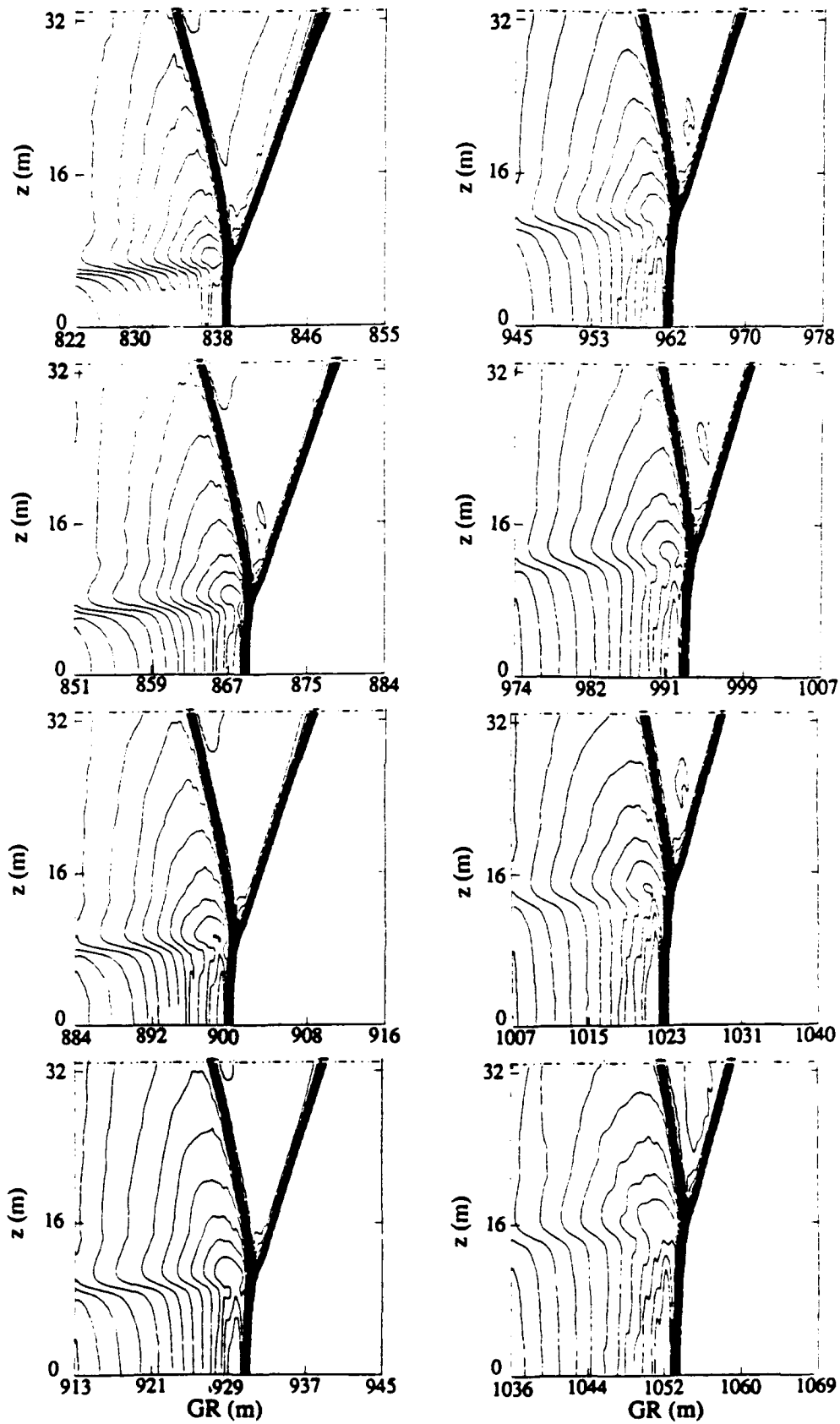


Figure 31. Entropy contours showing the reflection of a point-source blast wave from a plane; $HOB = 1056/KT^{1/3} = 322 \text{ m}/KT^{1/3}$ (Concluded).

APPENDIX

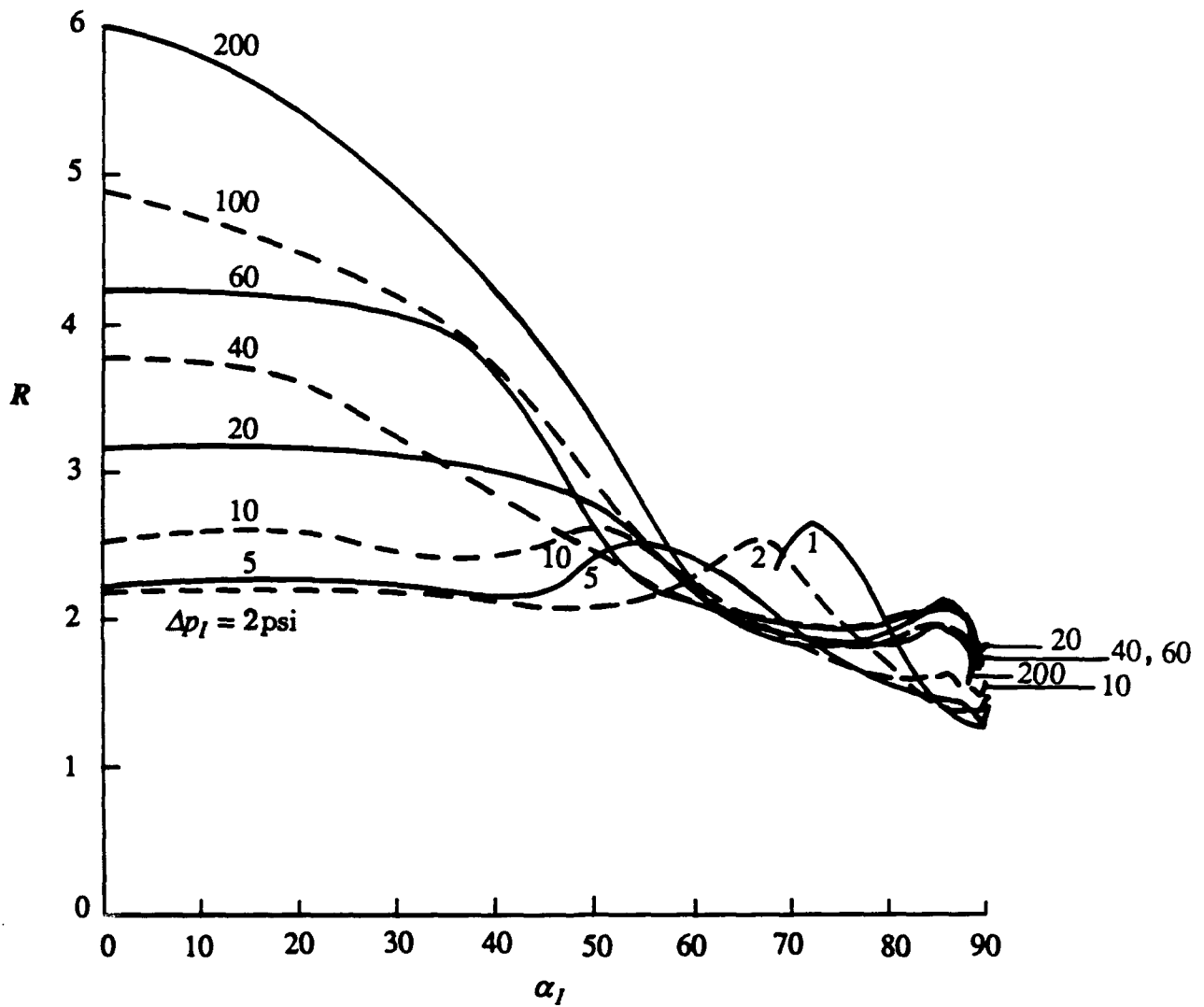


Figure A1. Height-of burst reflection factors from the NP experiments performed over the smooth (Makrolon) surface.

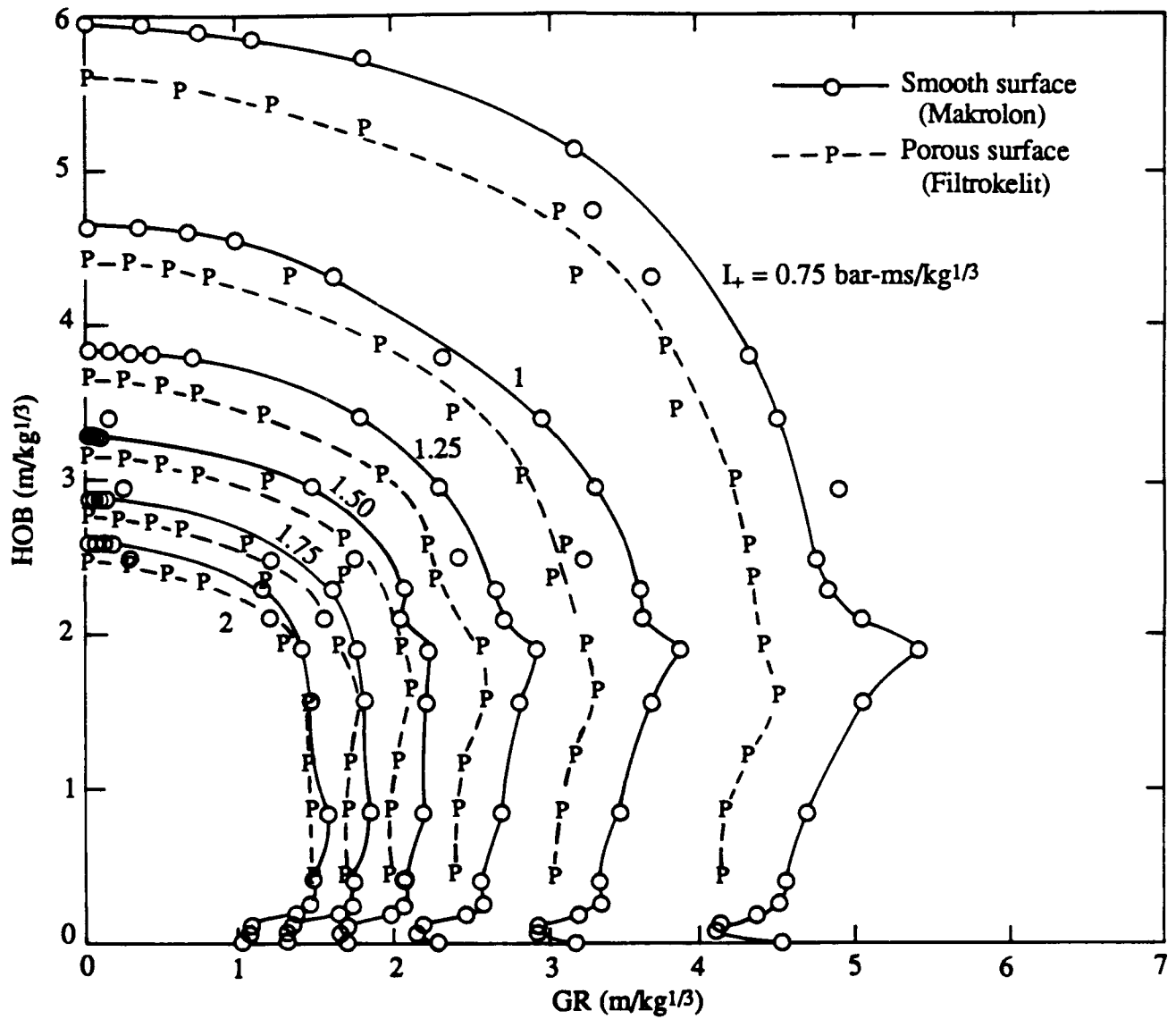


Figure A2. Comparison of the NP height-of-burst curves for positive phase impulse, L_+ , for a smooth surface vs. a porous surface.

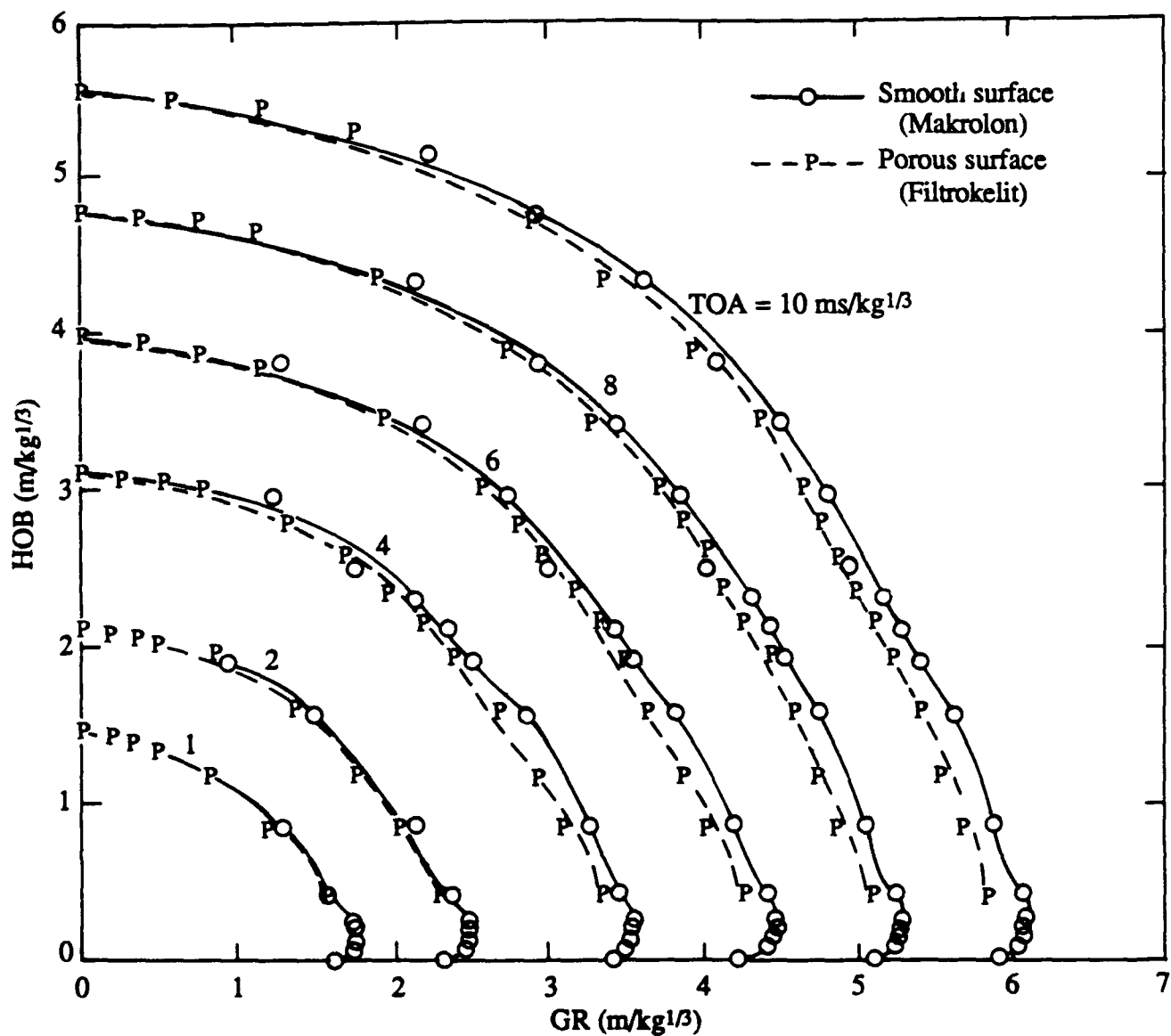


Figure A3. Comparison of the NP height-of-burst curves for shock arrival time, TOA, for a smooth surface vs. a porous surface.

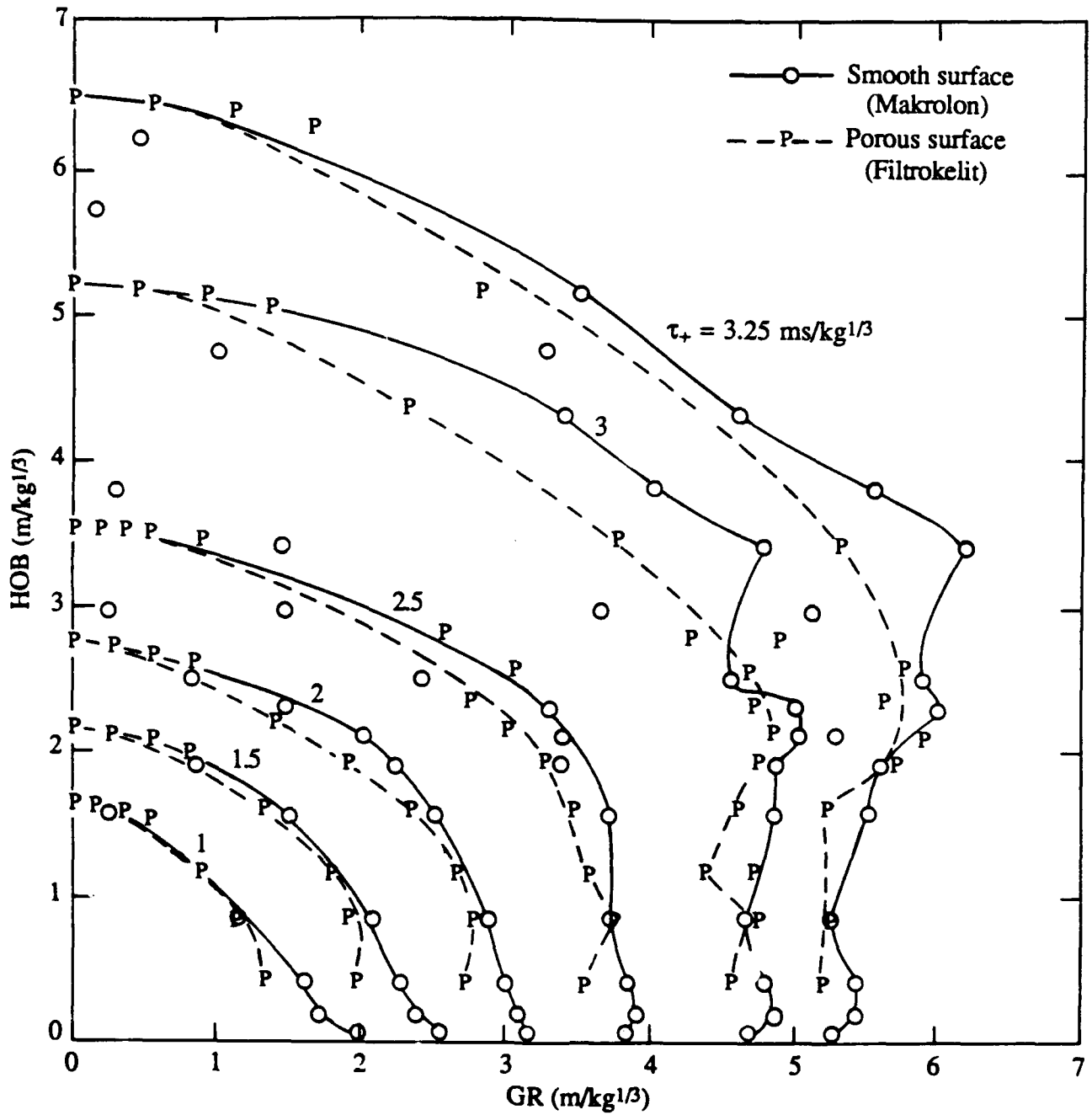


Figure A4. Comparison of the NP height-of-burst curves for positive phase duration, τ_+ , for a smooth surface vs. a porous surface.

DISTRIBUTION LIST

DNA-TR-90-223

DEPARTMENT OF DEFENSE

ASSISTANT TO THE SECRETARY OF DEFENSE
ATTN: EXECUTIVE ASSISTANT

DEFENSE INTELLIGENCE AGENCY
ATTN: DB-TPO

DEFENSE NUCLEAR AGENCY
ATTN: DDIR G ULLRICH
ATTN: OTA P ROHR
ATTN: SPSD
ATTN: SPSD LT COL ARTMAN
ATTN: SPSP P CASTLEBERRY
ATTN: SPWE C GALLOWAY
ATTN: SPWE K PETERSEN
ATTN: SPWE T FREDRICKSON
ATTN: TDTR
2 CYS ATTN: TITL

DEFENSE NUCLEAR AGENCY
ATTN: TDNV

DEFENSE NUCLEAR AGENCY
ATTN: ENIE N GANTICK
ATTN: TDNM
2 CYS ATTN: TDTT W SUMMA
ATTN: TTST E MARTINEZ
ATTN: TTST E RINEHART

DEFENSE TECHNICAL INFORMATION CENTER
2 CYS ATTN: DTIC/FDAB

DEPARTMENT OF DEFENSE EXPLO SAFETY BOARD
ATTN: CHAIRMAN

STRATEGIC AND THEATER NUCLEAR FORCES
ATTN: DR E SEVIN

THE JOINT STAFF
ATTN: JKC (ATTN: DNA REP)
ATTN: JKCS
ATTN: JLWD
ATTN: JPEN

DEPARTMENT OF THE ARMY

DEPT CH OF STAFF FOR OPS & PLANS
ATTN: DAMO-SWN

HARRY DIAMOND LABORATORIES
ATTN: SLCIS-IM-TL TECH LIB

U S ARMY ARMAMENT, MUNITIONS, & CHEM CMD
ATTN: MA LIBRARY

U S ARMY BALLISTIC RESEARCH LAB
2 CYS ATTN: SLCBR-SS-T TECH LIB

U S ARMY CORPS OF ENGINEERS
ATTN: CERD-L

U S ARMY ENGINEER DIV HUNTSVILLE
ATTN: HNDED-SY

U S ARMY ENGINEER DIV OHIO RIVER
ATTN: ORDAS-L TECH LIB

U S ARMY ENGR WATERWAYS EXPER STATION
ATTN: C WELCH CEWES-SE-R
ATTN: CEWES J K INGRAM
ATTN: CEWES-SD DR J G JACKSON, JR
ATTN: J ZELASKO CEWES-SD-R
ATTN: RESEARCH LIBRARY

U S ARMY FOREIGN SCIENCE & TECH CTR
ATTN: AIFRTA

U S ARMY MATERIAL TECHNOLOGY LABORATORY
ATTN: DRXMR J MESSALL
ATTN: TECHNICAL LIBRARY

U S ARMY NUCLEAR & CHEMICAL AGENCY
ATTN: MONA-NU D BASH

U S ARMY RESEARCH DEV & ENGRG CTR
ATTN: STRNC-YSD G CALDARELLA

U S ARMY STRATEGIC DEFENSE CMD
ATTN: CSSD-H-SA
ATTN: CSSD-H-SAV
ATTN: CSSD-SD-A

U S ARMY STRATEGIC DEFENSE COMMAND
ATTN: CSSD-SA-EV
ATTN: CSSD-SL

U S ARMY WAR COLLEGE
ATTN: LIBRARY

USA SURVIVABILITY MANAGEMENT OFFICE
ATTN: SLCSM-SE J BRAND

DEPARTMENT OF THE NAVY

NAVAL POSTGRADUATE SCHOOL
ATTN: CODE 1424 LIBRARY

NAVAL RESEARCH LABORATORY
ATTN: CODE 2627 TECH LIB
ATTN: CODE 4040 D BOOK
ATTN: CODE 4400 J BORIS

NAVAL SURFACE WARFARE CENTER
ATTN: CODE R44 P COLLINS
ATTN: CODE R44 R FERGUSON

NAVAL WEAPONS EVALUATION FACILITY
ATTN: CLASSIFIED LIBRARY

OFFICE OF CHIEF OF NAVAL OPERATIONS
ATTN: OP 03EG

OFFICE OF NAVAL RESEARCH
ATTN: CODE 1132SM

DEPARTMENT OF THE AIR FORCE

AIR UNIVERSITY LIBRARY
ATTN: AUL-LSE

DNA-TR-90-223 (DL CONTINUED)

BALLISTICS SYSTEMS DIVISION/MY
ATTN: ENSR
ATTN: MGER
ATTN: MYET G E LAMAR

HEADQUARTERS USAF/IN
ATTN: IN

PHILLIPS LABORATORY
ATTN: NTCA

STRATEGIC AIR COMMAND/XPSW
ATTN: T E DENESIA XPS

STRATEGIC AIR COMMAND/XRFS
ATTN: XRFS

USAF/LEEEU
ATTN: LEE

DEPARTMENT OF ENERGY

DEPARTMENT OF ENERGY
OFFICE OF MILITARY APPLICATIONS
ATTN: OMA DP-225

LAWRENCE LIVERMORE NATIONAL LAB
ATTN: C E ROSENKILDE
ATTN: J BELL L-316
ATTN: L-203 R SCHOCK
ATTN: L-81 R PERRETT

LAWRENCE LIVERMORE NATIONAL LABRATORY
ATTN: ALLEN KUHL

LOS ALAMOS NATIONAL LABORATORY
ATTN: REPORT LIBRARY

MARTIN MARIETTA ENERGY SYSTEMS INC
ATTN: DR C V CHESTER

SANDIA NATIONAL LABORATORIES
ATTN: A CHABAI DIV 9311
ATTN: DIV 9311 J S PHILLIPS
ATTN: DIV 9311 L R HILL
ATTN: TECH LIB 3141

OTHER GOVERNMENT

CENTRAL INTELLIGENCE AGENCY
ATTN: OSWR/NED

DEPARTMENT OF DEFENSE CONTRACTORS

AEROSPACE CORP
ATTN: H MIRELS
ATTN: LIBRARY ACQUISITION

APPLIED & THEORETICAL MECHANICS, INC
ATTN: J M CHAMPNEY

APPLIED RESEARCH ASSOCIATES
ATTN: R FLORY

APPLIED RESEARCH ASSOCIATES, INC
ATTN: J KEEFER
ATTN: N ETHRIDGE

APPLIED RESEARCH ASSOCIATES, INC
ATTN: J L BRATTON

APPLIED RESEARCH ASSOCIATES, INC
ATTN: R FRANK

APPLIED RESEARCH ASSOCIATES, INC
ATTN: J L DRAKE

BDM INTERNATIONAL INC
ATTN: E DORCHAK
ATTN: J STOCKTON

CALIFORNIA RESEARCH & TECHNOLOGY, INC
ATTN: LIBRARY

CALIFORNIA RESEARCH & TECHNOLOGY, INC
ATTN: J THOMSEN
ATTN: K KREYENHAGEN

CARPENTER RESEARCH CORP
ATTN: H J CARPENTER

E-SYSTEMS, INC
ATTN: TECH INFO CTR

FLUID PHYSICS IND
ATTN: R TRACI

GEO CENTERS, INC
ATTN: B NELSON

IIT RESEARCH INSTITUTE
ATTN: DOCUMENTS LIBRARY
ATTN: M JOHNSON

INFORMATION SCIENCE, INC
ATTN: W DUDZIAK

INSTITUTE FOR DEFENSE ANALYSES
ATTN: CLASSIFIED LIBRARY

KAMAN SCIENCES CORP
ATTN: L MENTE
ATTN: LIBRARY
ATTN: R RUETENIK

KAMAN SCIENCES CORP
ATTN: JOHN KIETH

KAMAN SCIENCES CORP
ATTN: D MOFFETT
ATTN: DASIAC
ATTN: E CONRAD

KAMAN SCIENCES CORPORATION
ATTN: DASIAC

LOCKHEED MISSILES & SPACE CO, INC
ATTN: TECH INFO CTR D COLL

LOGICON R & D ASSOCIATES
ATTN: B KILLIAN
ATTN: E FURBEE

LOGICON R & D ASSOCIATES
2 CYS ATTN: A L KUHL
ATTN: C K B LEE
ATTN: D SIMONS

ATTN: LIBRARY
ATTN: T A MAZZOLA

LOGICON R & D ASSOCIATES
ATTN: G GANONG
ATTN: J WALTON

LOGICON R & D ASSOCIATES
ATTN: E FURBEE
ATTN: J WEBSTER

LTV AEROSPACE & DEFENSE COMPANY
2 CYS ATTN: LIBRARY EM-08

MCDONNELL DOUGLAS CORPORATION
ATTN: R HALPRIN

MOLZEN CORBIN & ASSOCIATES, P.A.
ATTN: TECHNICAL LIBRARY

NEW MEXICO ENGINEERING RESEARCH INSTITUTE
ATTN: J JARPE
ATTN: N BAUM
ATTN: R NEWELL

NICHOLS RESEARCH CORP, INC
ATTN: R BYRN

PACIFIC-SIERRA RESEARCH CORP
ATTN: H BRODE
ATTN: L SCHLESSINGER
ATTN: L E JOUHNSON

PDA ENGINEERING
ATTN: J E WUERER

PHYSICAL RESEARCH INC
ATTN: D MODARRESS

RAND CORP
ATTN: B BENNETT

S-CUBED
ATTN: C PETERSEN
ATTN: G SCHNEYER
ATTN: J BARTHEL
ATTN: K D PYATT, JR
ATTN: P COLEMAN
ATTN: T PIERCE

S-CUBED
ATTN: C NEEDHAM

SCIENCE APPLICATIONS INTL CORP
ATTN: C HSIAO
ATTN: F Y SU
ATTN: G EGGUM

ATTN: G T PHILLIPS
ATTN: H WILSON
ATTN: TECHNICAL REPORT SYSTEM

SCIENCE APPLICATIONS INTL CORP
ATTN: DIV 411 R WESTERFELDT

SCIENCE APPLICATIONS INTL CORP
ATTN: J WILLIAMS

SCIENCE APPLICATIONS INTL CORP
ATTN: J COCKAYNE
ATTN: W LAYSON

SCIENCE APPLICATIONS INTL CORP
ATTN: K SITES

SCIENCE APPLICATIONS INTL CORP
ATTN: G BINNINGER

SCIENCE APPLICATIONS INTL CORP
ATTN: R ALLEN

SRI INTERNATIONAL
ATTN: D KEOUGH
ATTN: J COLTON
ATTN: J SIMONS
ATTN: M SANAI

TECHNICO SOUTHWEST INC
ATTN: S LEVIN

TRW INC
ATTN: M SEIZEW

TRW SPACE & DEFENSE SECTOR
ATTN: HL DEPT LIBRARY
ATTN: OUT6 W WAMPLER

WASHINGTON STATE UNIVERSITY
ATTN: PROF Y GUPTA

WEIDLINGER ASSOC, INC
ATTN: H LEVINE

WEIDLINGER ASSOCIATES, INC
ATTN: T DEEVY

WEIDLINGER ASSOCIATES, INC
ATTN: I SANDLER
ATTN: M BARON

FOREIGN

ERNST-MACH-INSTITUT
2 CYS ATTN: C SCHEKLINKSI-GLUCK
2 CYS ATTN: H REICHENBACH